A&A, 710, A66 (2026)
https://doi.org/10.1051/0004-6361/202558287

Astronomy & Astrophysics

Unravelling the complex structure of the Fe II emission region in Type 1 active galactic nuclei

Jelena Kovačević-Dojčinović[1,⋆], Ivan Dojčinović[2,⋆], and Luka Č. Popović[1,3,⋆]

[1] Astronomical Observatory, Volgina 7, 11160 Belgrade, Serbia
[2] Faculty of Physics, University of Belgrade, Studentski Trg 12, 11000 Belgrade, Serbia
[3] Department of Astronomy, Faculty of Mathematics, University of Belgrade, Studentski Trg 16, 11000 Belgrade, Serbia

Received 27 November 2025 / Accepted 9 April 2026

ABSTRACT

Aims. Using a large sample of Type 1 active galactic nucleus spectra, we investigated the complex structure of the Fe II emission region with the aim of understanding the atomic processes responsible for the enhancement of the Fe II emission. We explored correlations between Fe II features and other spectral parameters, with special focus placed on the quasar main sequence, whose underlying physics is crucial for understanding the origin of the strong Fe II emission.

Methods. The Fe II emission was modelled using the flexible Fe II template that decomposes the optical Fe II lines into several line groups. According to the atomic properties of transitions, the Fe II lines were divided into inconsistent and consistent groups (Fe II_{incons} and Fe II_{cons}), while Fe II_{cons} lines were additionally decomposed into components originating from different parts of the broad-line region (Fe II_{ILR} and Fe II_{VBLR}). We traced the behaviour of these line groups and components along the quasar main sequence.

Results. Anti-correlation between the equivalent width (EW) of Fe II and the full width at half maximum of Fe II appears to be a more fundamental relation underlying the quasar main sequence. The increase in the EW Fe II for smaller line widths is primarily caused by the strengthening of the EW Fe II_{incons} lines and, with a smaller contribution, by the enhancement of the EW Fe II_{ILR} components, while the EW of Fe II_{VBLR}, on average, does not significantly change along the quasar main sequence. The results indicate a possible stratification of the Fe II emission region occurring in sources with strong Fe II emission. An increased Eddington ratio may modify the broad-line region structure, leading to the formation of localised regions with specific physical conditions suitable for triggering additional atomic processes. This may result in the appearance of Fe II_{incons} lines and Fe II_{ILR} components, which consequently increase the optical Fe II strength.

Key words. line: formation – line: profiles – galaxies: active – quasars: emission lines

1. Introduction

The spectra of Type 1 active galactic nuclei (AGNs) exhibit remarkable diversity in the strength and shape of Fe II emission features, reflecting the complex structure and physical conditions within the broad-line region (BLR). Numerous correlations have been reported between the Fe II emission lines and other spectral parameters, although their physical origin remains unclear. Among the most significant and extensively studied is the anti-correlation between the Fe II/Hβ ratio and the width of the Hβ line, which was first observed in several early works (Gaskell 1985; Zheng & O'Brien 1990; Zheng & Keel 1991).

Boroson & Green (1992) applied the principal component analysis (PCA) to various observed spectral features, and eigenvector 1 (EV1) of their PCA revealed a significant relationship between several spectral parameters. Among the strongest and the most intriguing correlations of EV1 are the aforementioned anti-correlation between the Fe II/Hβ ratio (hereafter R_{FeII}) and the full width at half maximum (FWHM) of Hβ as well as the anti-correlation between R_{FeII} and the equivalent width (EW) of the [O III]$\lambda\lambda$ 4959, 5007 Å lines (Boroson & Green 1992). Sulentic et al. (2000a) proposed that the observed diversity among quasars can be organised in the so-called quasar main sequence, which in the optical plane is represented by the R_{FeII} – FWHM Hβ anti-correlation (Sulentic et al. 2000b; Marziani et al. 2001; Sulentic et al. 2007; Marziani et al. 2018). Based on the characteristic distribution of sources in the R_{FeII}–FWHM Hβ anti-correlation, Sulentic et al. (2000a,b) introduced the concept of two distinct quasar populations, A and B, separated at the FWHM Hβ = 4000 km s^{-1}. It has been suggested that this division represents a real physical dichotomy among AGNs (Sulentic et al. 2011). The underlying physical processes responsible for the R_{FeII}–FWHM Hβ anti-correlation have been debated extensively over the past decades. Boroson & Green (1992) proposed that EV1 in their PCA and accordingly the R_{FeII}–FWHM Hβ anti-correlation are driven predominantly by the Eddington ratio. Several later studies concluded that the underlying physics of the EV1 is primarily governed by the Eddington ratio in combination with orientation (Sulentic et al. 2000a; Marziani et al. 2001; Shen & Ho 2014). There have been many attempts to theoretically reproduce and model the R_{FeII}–FWHM Hβ anti-correlation using spectral synthesis code CLOUDY (Panda et al. 2018, 2019a,b; Floris et al. 2024). Results from modelling indicate that this anti-correlation depends on a combination of many physical parameters, including the Eddington ratio, black hole mass, BLR density and metallicity, micro-turbulence, and orientation (see Panda 2024).

The most intriguing objects are located at the extreme end of Population A in the quasar main sequence, showing narrow Hβ lines, and the strongest R_{FeII} (the so-called extreme population

⋆ Corresponding authors: jkovacevic@aob.bg.ac.rs; lpopovic@aob.bg.ac.rs; ivan.dojcinovic@ff.bg.ac.rs

A) (see Marziani et al. 2025). These very strong Fe II emitters exhibit several important spectral characteristics that are not yet fully understood and remain difficult to reproduce within the framework of established BLR models. In these objects, the observed ratio of the optical Fe II to the UV Fe II lines is significantly higher than theoretically predicted, and several excitation mechanisms and atomic processes have been proposed to explain it (see e.g. Joly 1981; Sigut & Pradal 1998; Collin & Joly 2000). The model assuming a large optical depth and high column density for the UV Fe II lines provides the closest agreement with the observed values of this ratio (Collin-Souffrin et al. 1980; Joly 1981), suggesting that self-absorption of the UV Fe II lines has an important role in the enhancement of the optical Fe II emission relative to the UV Fe II. One of the proposed explanations for the excess of optical Fe II emission observed in these spectra is an enhanced iron abundance in the BLR, corresponding to super-solar metallicity (Baldwin et al. 2003; Negrete et al. 2012; Panda et al. 2019a; Śniegowska et al. 2021).

Reproducing the observed optical-to-UV Fe II ratio as well as the relative intensities among optical Fe II lines in strong Fe II emitters remains challenging even for the most advanced photoionisation models that incorporate extensive atomic datasets (Zhang et al. 2024; Pandey et al. 2025). However, in most cases, modelling studies of strong Fe II emitters assume that the Fe II lines originate in a single emission region with specific physical parameters without any stratification. Possible stratification in the Fe II emission region was investigated by Popović et al. (2023), who constructed a sample of model spectra assuming a two-component BLR consisting of two layers with different physical properties: a very broad line region (VBLR) located closer to the black hole and an intermediate-line region (ILR) located further away from the black hole. This sample of synthetic spectra with different ILR and VBLR contributions in Hβ and Fe II lines succeeded in reproducing the quasar main sequence, where both parameters in this anti-correlation (R_{FeII} and FWHM Hβ) were found to depend strongly on the relative contributions from the ILR and VBLR.

The spectra with strong and narrow Fe II lines have one more particularity apart from the flux excess of optical Fe II relative to UV Fe II lines. The relative intensities among optical Fe II lines do not follow theoretically calculated values (Véron-Cetty et al. 2004; Zhang et al. 2024). Namely, some optical Fe II lines that are expected to be very weak and hardly visible in the spectra according to their transition probabilities in strong Fe II emitters can be up to two orders of magnitude stronger than predicted. Their observed intensities become comparable to those of other optical Fe II lines with much higher transition probabilities (see Kovačević-Dojčinović et al. 2025). Kovačević-Dojčinović et al. (2025) investigated these optical Fe II lines and referred to them as inconsistent Fe II lines (Fe II_{incons}), alluding to the inconsistency between their measured intensities in the spectra and the theoretically expected values. The Fe II lines whose relative intensities follow the theoretically predicted values were referred to as consistent Fe II lines (Fe II_{cons}). They found that as the Eddington ratio increases and as the line widths decrease, the intensity of the Fe II_{incons} lines increases relative to Fe II_{cons}, and at the same time, the total optical Fe II emission increases relative to UV Fe II emission. They also found that some of the Fe II_{incons} lines are narrower than Fe II_{cons} and suggested that the Fe II spectrum is likely a complex mixture of radiation originating from emission regions with different physical conditions and distances from the black hole.

All of these results indicate that optical Fe II lines have a complex origin and should be dissected in order to understand their role in the quasar main sequence and in the other unexplained correlations. Therefore, in this study, we applied the complex Fe II template presented in Kovačević-Dojčinović et al. (2025) to analyse the properties of the optical Fe II lines in a large sample of AGN spectra. This template decomposes the optical Fe II lines into several line groups according to the atomic properties of their transitions, thus allowing for a separate analysis of the inconsistent and consistent Fe II lines. We followed the variations in the relative intensities between the Fe II_{incons} and Fe II_{cons} lines along the quasar main sequence as well as changes in the contribution of the Fe II emission from the ILR and VBLR. In this way, we sought to obtain a better understanding of the physical processes responsible for the strong Fe II emission and to explain the physics underlying the quasar main sequence.

In Sect. 2, we describe our sample and the method of spectral decomposition. The results are presented in Sect. 3 and discussed in Sect. 4. Finally, our conclusions are summarised in Sect. 5.

2. Sample and analysis

Kovačević-Dojčinović et al. (2025) used the sample of 1046 Type 1 AGN spectra for investigation of the Fe II emission lines and atomic processes involved in their emission. Since that sample is well defined and chosen to have high-quality spectra convenient for sophisticated spectral decomposition and analysis, we used the same sample for this research. Detailed description of the sample selection, spectral correction for reddening, redshift and host galaxy contribution, as well as fitting procedure, is given in Kovačević-Dojčinović et al. (2025). Here we list the most important steps in that process.

The sample is taken from Sloan Digital Sky Survey (SDSS) database, Data Release 16 (DR16) (Ahumada et al. 2020) using structural query language (SQL) in order to satisfy the following criteria: objects to be Type 1 AGNs, cosmological redshift (z) to be $z < 0.7$ and with no redshift warning, and median S/N per pixel of the whole spectrum and g-band to be greater than 30. In this way we got the high-quality spectra which cover optical Fe II emission in the 4000–5600 Å range, in which Fe II lines can be precisely fitted. For correction of the Galactic extinction, we used the standard extinction law given in Howarth (1983) and extinction coefficients given in Schlegel et al. (1998). After correction for the cosmological redshift, we decomposed the spectra to the host and pure-AGN contribution using the method of the spectral PCA, as it is described in Vanden Berk et al. (2006). In this method we fitted the spectra with the linear combination of two independent sets of eigenspectra, derived from the pure-quasar (Yip et al. 2004a) and the pure-galaxy (Yip et al. 2004b) SDSS samples. The host galaxy contribution is obtained as the linear combination of only pure-galaxy eigenspectra, obtained from the best fit. The pure-AGN spectra are obtained after subtraction of the host galaxy contribution from the observed spectra. The example of the spectral decomposition to the host galaxy and the pure-AGN contribution could be seen in Kovačević-Dojčinović et al. (2025) (see their Fig. 1).

Afterwards, the pure AGN spectra were fitted with the multi-Gaussian model. In applied fitting procedure all emission lines in 4000–5600 Å range and continuum emission were fitted simultaneously. The continuum is modelled with power-law, while emission lines were modelled with single or multiple Gaussian functions. The Balmer lines in 4000–5600 Å range were fitted with three Gaussian components: one narrow Gaussian that fits the emission from the narrow-line region (NLR), while emission from BLR is described with sum of the two broad

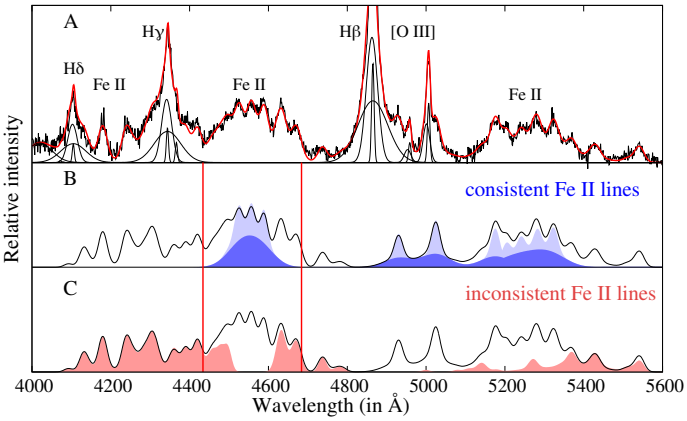

Fig. 1. Example of the spectral decomposition in the 4000–5600 Å range. Panel A shows the multi-Gaussian decomposition for SDSS J111941.12+595108.7, where the best fit is denoted with a red line. The Fe II template is shown separately as black solid line in Panels B and C. In Panel B, the consistent Fe II lines are shaded with the blue colour. The sum of the ILR components is coloured with light blue, and sum of the VBLR components in dark blue. In Panel C, the inconsistent Fe II lines are coloured with red. Two vertical red lines in Panels B and C denote the spectral range of 4434–4684 Å, usually used for calculation of the R_{FeII}.

Gaussians, as we assume that broad component of the Balmer lines originate from two layers of the BLR. One is the ILR, which is supposed to be outermost area of the BLR, farther away from the black hole. The emission from this region is represented with Gaussian that fits the core of the broad lines. The other sub-region is VBLR, which is the inner layer of the BLR and is represented with broader Gaussian which fits wings of the lines. This two-Gaussian decomposition approach for BLR emission is commonly used for spectra with very broad Balmer lines (see e.g. Hu et al. 2008; Li et al. 2015). However, several studies have shown that Lorentzian profiles provide a good fit of the broad emission-line shapes in the case of the NLSy1 galaxies, and more generally in Population A sources (see e.g. Véron-Cetty et al. 2001; Sulentic et al. 2002). We find that the broad Balmer line profiles in NLSy1 galaxies can be also very well reproduced by the sum of two Gaussian components resulting in the 'Lorentzian-like' shape. We therefore interpret the broad Balmer line shapes in NLSy1s as the superposition of Gaussian components with different widths, reflecting Doppler broadening in distinct BLR layers, rather than a single Lorentzian profile, which is expected to arise by some other broadening mechanism (collisional broadening, Stark broadening, etc.). This approach allowed us to apply a uniform Balmer-line decomposition model across the entire AGN sample, independent of Balmer line widths, while preserving a consistent physical interpretation of Doppler broadening as the dominant mechanism affecting broad-line AGN profiles. The widths and shifts of the ILR Gaussians are fixed to be the same for all Balmer lines within one spectrum. The same is done for the widths and shifts of the VBLR Gaussians and ILR/VBLR intensity ratio. Additionally, the relative intensities of the broad components of Hβ, Hγ and Hδ lines are fixed to follow the theoretical value for case B (see Osterbrock & Ferland 2006).

The numerous Fe II lines are fitted with the Fe II model given in Kovačević-Dojčinović et al. (2025), which is the improved version of the Fe II template given in Kovačević et al. (2010) (see more details in Sect. 2.1). The narrow lines in 4000–5600 Å range (narrow Balmer components, [O III] 4959, 5007 Å, [O III] 4363 Å and [S II] 4068, 4076 Å) are fitted with single Gaussian components, with the same widths and shifts. In the case of observed asymmetry in [O III] 4959, 5007 Å profile, additional wing component is included in the modelling of these lines. The He II 4686 Å and He I 4026 Å lines are fitted with single broad Gaussians. The example of the spectral decomposition in 4000–5600 Å range is given in Figure 1, Panel A.

2.1. Flexible Fe II Template: A tool for investigation of the complex Fe II emission

Several studies have shown that the relative intensities among Fe II multiplets vary in different AGN spectra (Kovačević et al. 2010; Shapovalova et al. 2012; Ilić et al. 2023; Kovačević-Dojčinović et al. 2025). Therefore, empirical Fe II templates with fixed relative intensities among Fe II lines cannot accurately fit Fe II emission in the case of spectra with significantly different Fe II properties (see appendix in Kovačević et al. 2010; Kovačević-Dojčinović et al. 2025). The semi-empirical Fe II model given in Kovačević et al. (2010) separate the Fe II lines into several line groups according to atomic properties of transitions, giving them the free parameter of intensity, achieving in this way the flexibility of the model and possibility for analysis of atomic processes. As a result, the template gives the intensities of the different Fe II line groups, following the 'breathing' of the Fe II lines in different spectra. Kovačević-Dojčinović et al. (2025) upgraded and improved the Fe II model given in Kovačević et al. (2010) by addressing some deficiencies of initial model and giving more degrees of freedom for fitting the complex Fe II emission. These modifications result in a more accurate fit of Fe II lines that can successfully reproduce Fe II emission of various properties. The great flexibility of this template also allows for investigation of the behaviour of a certain group of Fe II lines, giving a better insight into the complex physics of Fe II emission.

In the Fe II model given in Kovačević-Dojčinović et al. (2025), the Fe II lines in 4000–5600 Å range are divided into two large groups. The first group comprises the lines whose observed relative intensities follow the values obtained by theoretical calculations using their atomic parameters (so-called consistent Fe II lines, Fe II_{cons}). The other group contains those lines whose observed relative intensities could be significantly larger than theoretically expected. These lines are addressed as inconsistent Fe II lines (Fe II_{incons}), which alludes to the inconsistency of their measured intensities with theoretically predicted. While the consistent Fe II lines arise from allowed transitions, the inconsistent Fe II lines are mostly intersystem and intercombination multiplets, with the addition of several forbidden multiplets, allowed lines and several transitions originating from highly excited levels. Most of Fe II_{incons} lines have up to two orders of magnitude lower Einstein coefficients for spontaneous emission comparing the Fe II_{cons}. Consequently, they should be barely detectable in optically thin spectra, even when Fe II_{cons} lines are very strong. However, in some spectra their intensities are comparable to those of the consistent Fe II lines, suggesting that additional atomic processes enhance their emission. Most of Fe II_{incons} lines share the same upper transition level as Fe II_{cons} lines, while the lower levels of both groups have similar energies and are all metastable. One of the possible mechanisms which may increase intensities of the Fe II_{incons} lines could be the self-absorption of Fe II_{cons} lines. Since Fe II_{incons} lines have significantly lower emission and absorption probabilities than Fe II_{cons}, and both have lower metastable levels, the process

of self-absorption would be more efficient for Fe II_{cons} lines and would lead to a redistribution of energy from Fe II_{cons} to the Fe II_{incons} lines, thereby increasing the intensities of Fe II_{incons} (see Kovačević-Dojčinović et al. 2025).

The consistent Fe II lines were divided into three line groups (F, S, and G) formed following their lower term of transition. The intensities of the line groups were set to be the free parameters, while the relative intensities among the Fe II lines within these groups were calculated using formula 1 in Kovačević et al. (2010). The widths of the Fe II lines are strongly correlated with those of the broad Balmer lines (Kovačević et al. 2010; Kovačević-Dojčinović & Popović 2015), indicating important role of Doppler broadening in shaping of their profiles. Therefore, we initially applied the same two-component approach used for the broad Balmer lines to model the Fe II line profiles across the entire sample. The consistent Fe II lines, which are the strongest in Fe II bump, were fitted with a two-Gaussian model, where the ILR component fits the core and the VBLR component fits the wings of the lines, assuming that these components arise in kinematically distinct layers of the BLR. We assumed that the widths of ILR and VBLR components as well as their intensity ratio are the same for all Fe II consistent lines within one spectrum. None of these parameters were tied with the same parameters of the Balmer lines in the fitting procedure. In Appendix A, we analyse the justification for using a two-component model for fitting of Fe II_{cons} lines, and we found that this approach provides a significantly better fit for spectra with narrower Fe II lines, where individual line peaks are visible within the Fe II bump. However, for spectra with very broad Fe II lines, with approximately FWHM Fe II > 5000 km s^{-1}, its application does not improve the fit (see Figure A.1). In these spectra, the Fe II lines form smooth bumps without distinguishable Fe II line peaks, so both the ILR and VBLR Gaussians overlap, as they have very broad and similar widths. This is not in accordance with the assumptions of the two-component model, which predicts that the ILR components have significantly narrower widths than the VBLR components, as they originate from kinematically different regions. Therefore, the two-component Fe II model was applied only for spectra with estimated width of Fe II lines smaller than 5000 km s^{-1}. For spectra with FWHM Fe II > 5000 km s^{-1}, the Fe II emission lines were fitted with a single Gaussian model for each Fe II line, assuming that all Fe II emission arises from a kinematically uniform emission region with very high Doppler velocities. An example of the Fe II decomposition for a spectrum with FWHM Fe II < 5000 km s^{-1}, where consistent Fe II lines are fitted with two-component model, is shown in Figure 1, Panel B.

The inconsistent Fe II lines were divided into four line groups (P+, G+, H and OL), following the atomic characteristic of their transitions and similar behaviour in spectra. Each of the line groups has the free parameter of intensity, while the relative intensities among the lines within groups were fixed since they are determined empirically (see Kovačević-Dojčinović et al. 2025). The inconsistent Fe II lines were fitted with single Gaussian model, and each group has a free parameter for width. The shift was taken to be the same for all Fe II lines in model. The inconsistent Fe II lines are highlighted in Figure 1, Panel C.

To summarise, in the complex Fe II model, the intensities of consistent lines are described with five parameters. These are three parameters of intensity for F, S, and G line groups, temperature for calculation of the relative intensities of lines within the groups, and one parameter for intensity ratio of VBLR/ILR components. The other free parameters that describe the consistent Fe II lines are the widths of ILR and VBLR components and the shift. The inconsistent Fe II lines are described with free parameter of intensity and width for each of line groups (P+, G+, OL and H). All consistent and inconsistent Fe II line groups with a free intensity parameter have at least some lines that do not overlap with the lines from the other line groups. This enables a reliable determination of their fluxes and reduces the possibility of flux redistribution among them due to fitting degeneracies. Detailed explanation of complex Fe II model, with summarised properties and list of the included lines in different line groups, is given in Kovačević-Dojčinović et al. (2025) (see their Appendix B).

2.2. Measurements of spectral properties and error estimates

For purpose of this research we measured FWHMs, EWs and fluxes of Hβ and Fe II lines. The FWHM of the broad Hβ is measured using the sum of the ILR and VBLR Hβ components, obtained from the best fit. Maximum of the sum is normalised to the unit, and the width at half intensity is measured. The dispersion of the broad Hβ line was computed as the flux-weighted second moment of the total broad line profile (Peterson et al. 2004).

Since the Fe II_{cons} are also fitted with two-Gaussian model for spectra where Fe II width is smaller than 5000 km s^{-1}, their FWHM is measured in the same manner as for Hβ. We singled out one Fe II consistent line, which is the sum of the ILR and VBLR Fe II components. We normalised it to unity and measured the width at half maximum of its overall shape as illustrated in Figure 2. The FWHMs of the inconsistent Fe II line groups are obtained directly from the best fit, as well as the widths of the consistent Fe II lines broader than 5000 km s^{-1}, which are fitted with a single-Gaussian model. The consistent Fe II lines are present in all objects with observed Fe II lines, which is 1022 objects from total sample, while majority of inconsistent Fe II lines disappear in spectra with broader emission lines (FWHM > 5000 km s^{-1}) (see Kovačević-Dojčinović et al. 2025). Therefore, in this work we use only the measured width of the consistent Fe II lines, in further text assigned as FWHM Fe II. The flux and EW of Hβ are measured for a total broad line. In the case of Fe II, the flux and EW are measured for the sum of the multiple lines: all consistent Fe II (Fe II_{cons}), all inconsistent Fe II (Fe II_{incons}) and for all Fe II lines in 4000–5600 Å range (Fe II_{cons}+Fe II_{incons}), denoted as Fe II_{tot}. In the case of the Fe II_{cons}, the fluxes and EWs are also separately measured for sum of their ILR (Fe II_{ILR}) and VBLR (Fe II_{VBLR}) components (see Figure 1, Panel B).

For accurate measuring of the fluxes and specially EWs of the lines, the correct determination of the continuum level is very important. Popović et al. (2023) found that in the case of spectra with strong and very broad Fe II lines, the optical Fe II quasi-continuum can be very strong, and it is difficult to separate it from the power-law continuum. It can cause the effect of underestimated fluxes of the Fe II and Hβ lines and slightly overestimated flux of continuum under these lines. Consequently, the most affected measured parameters are the EWs, especially EW of Fe II, which may be strongly underestimated, in the case of the strong Fe II pseudocontinuum. In order to reduce the uncertainty in the determination of continuum level caused by Fe II pseudocontinuum, we have taken several steps in fitting procedure (see Appendix A in Kovačević-Dojčinović et al. 2025). The most important steps are simultaneously fitting of the continuum power-law with the emission lines, fixing the relative intensities of the Balmer lines to follow theoretical values for case B, and including of two-Gaussian model for consistent Fe II lines in the

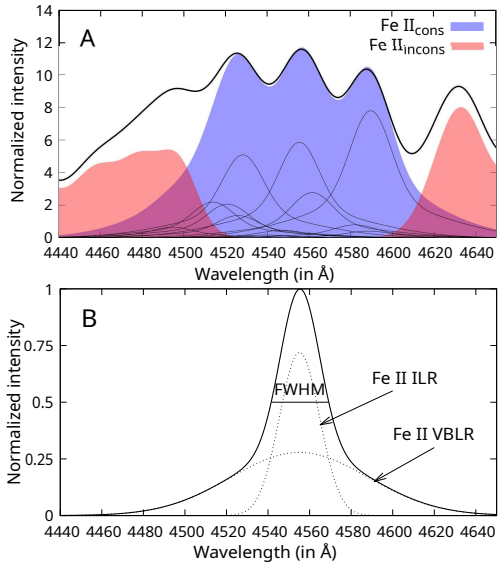

Fig. 2. Measuring the FWHM of Fe II$_{cons}$ lines fitted with the two-Gaussian model. Panel A: Sum of Fe II$_{cons}$ lines. The Fe II$_{cons}$ lines are shown with a solid thin lines, while their sum is coloured in blue. Panel B: Single Fe II$_{cons}$ line. We extracted one Fe II$_{cons}$ line (λ4549.5 Å), which consists of the sum of the ILR and VBLR components, and measured the FWHM of the entire line profile.

case of sources where the application of that model is justified. The EWs of Hβ and Fe II lines are measured relative to continuum under these lines.

The bolometric luminosity (L_{bol}) was calculated as $L_{bol} = 9 \cdot \lambda L_{5100}$ (Kaspi et al. 2000) and the Eddington luminosity (L_{Edd}) as $L_{Edd} = 1.26 \cdot 10^{38} (M_{BH}/M_{sun})$ erg s^{-1} (Wu & Liu 2004). The Eddington ratio (R_{Edd}) was estimated as $R_{Edd} = L_{bol}/L_{Edd}$. The adopted cosmological parameters for luminosity calculation were $\Omega_M = 0.3$, $\Omega_\Lambda = 0.7$, and $\Omega_k = 0$, and a Hubble constant of $H_0 = 70$ km s^{-1} Mpc^{-1} was assumed.

We estimated the fitting uncertainties using a Monte Carlo method. Since we applied a different Fe II modelling approaches for spectra with narrow and very broad Fe II lines, we divided the total sample into two subsamples, with the division set at an FWHM Fe II = 5000 km s^{-1}. We calculated the mean spectrum for each subsample by normalising the spectra at the same continuum level at λ5630 Å. Then, we created two subsets of 100 mock spectra by adding random noise to the mean spectra. The level of noise in mock spectra is taken to be as in the spectrum with the highest measured noise in the sample. In this way we wanted to estimate the upper limit of uncertainties. After fitting procedure, we took the 1σ dispersion of the parameters as the parameter uncertainty, similarly as done in Kovačević-Dojčinović et al. (2025). For spectra with an FWHM Fe II less than 5000 km s^{-1}, we estimated the following uncertainties: ∼5% for FWHMs of Hβ and Fe II, and up to ∼6% for all measured fluxes (Fe II$_{tot}$, Fe II$_{cons}$, Fe II$_{incons}$, Fe II ILR and VBLR components, narrow and broad components of Hβ and [O III]λ5007 Å). The upper limit on the uncertainties in the shifts of the narrow lines and [O III] wing components is ∼5%. For spectra with FWHM Fe II larger than 5000 km s^{-1}, parameter uncertainties are: ∼7% for FWHMs of Hβ and Fe II, and up to ∼7% for all measured fluxes of lines. The upper error in shift of the narrow lines and [O III] wing components is ∼6%. The uncertainties of the EWs are estimated as 1σ dispersion of the measured EWs of the lines for 100 mock spectra, in each subsample. For the subsample with an FWHM Fe II less than 5000 km s^{-1}, we obtained uncertainties up to ∼6% for all measured EWs of lines and their components, and for spectra with an FWHM Fe II greater than 5000 km s^{-1}, we obtained uncertainties up to ∼7%.

Since we used a two-component model for decomposition of the consistent Fe II lines for a subsample with an FWHM Fe II smaller than the threshold of 5000 km s^{-1}, we investigated if objects near ∼5000 km s^{-1} may switch between decomposition models due to noise. For spectra with FWHM Fe II near the 5000 km s^{-1}, the upper limit for uncertainty is 7%, corresponding to 5000 ± 350 km s^{-1}. In our sample, 22 objects fall within this range, where placement into one of the two subsamples is uncertain. Since this represents only a small fraction of the total sample of 1022 spectra, we conclude that these uncertainties do not significantly affect our analysis.

We also investigated possible parameter degeneracies due to noise, testing whether part of the Fe II flux could be traded against the continuum emission or redistributed among different Fe II components during the fitting procedure. We searched for correlations between the flux residuals, defined as the difference between the fluxes measured in the mock spectra and those of the input model. We found a moderate anti-correlation between the residuals of the total Fe II flux and the continuum level for the mock spectra generated from both models (with narrower and with broader Fe II lines). For the mock spectra generated from the model with narrower Fe II lines, we also found a moderate anti-correlation between the residuals of the ILR and VBLR Fe II components. These anti-correlations indicate a partial flux redistribution between these components induced by the noise. These effects are accounted for in the estimated flux uncertainties, which do not exceed 7% for the fluxes of different Fe II components. No correlation is found between the flux residuals of the consistent and inconsistent Fe II lines.

3. Results

3.1. Quasar main sequence: Searching for the underlying correlation

We investigated in more details the quasar main sequence (Fe II/Hβ versus FWHM Hβ correlation), using the Fe II parameters obtained from the best fit with complex Fe II model. The flux ratio of Fe II and Hβ in this relationship is usually assigned as R_{FeII} parameter, and it represents the ratio of the integrated flux of Fe II in 4434–4684 Å range, and the flux of the broad component of Hβ. The FWHM Hβ is also measured only for the broad component of the line, after removal of the narrow component. Since this relationship is complex, with three spectral parameters included (Fe II and Hβ fluxes and the Hβ width), we tried to simplify it, and to find the underlying correlation, which can give more clues about the physics of the emission region. Through this analysis, we used the Spearman rank correlation coefficient, which is sensitive to monotonic relationships without assuming linearity and is less affected by outliers, making it appropriate for analysis of non-linear parameter dependencies.

In Figure 3(a), we plot the quasar main sequence for our sample. As expected, we found the negative correlation between these parameters (r = –0.34, P-value = 0, where r is the Spearman coefficient of correlation). If we take the larger spectral range of the integrated Fe II flux (4000–5600 Å, in further text Fe II$_{tot}$), instead narrow range of 4434–4684 Å, the coefficient of correlation does not change. Since our Fe II template allows the FWHM of the Fe II lines to be obtained (see Section 2.2), we

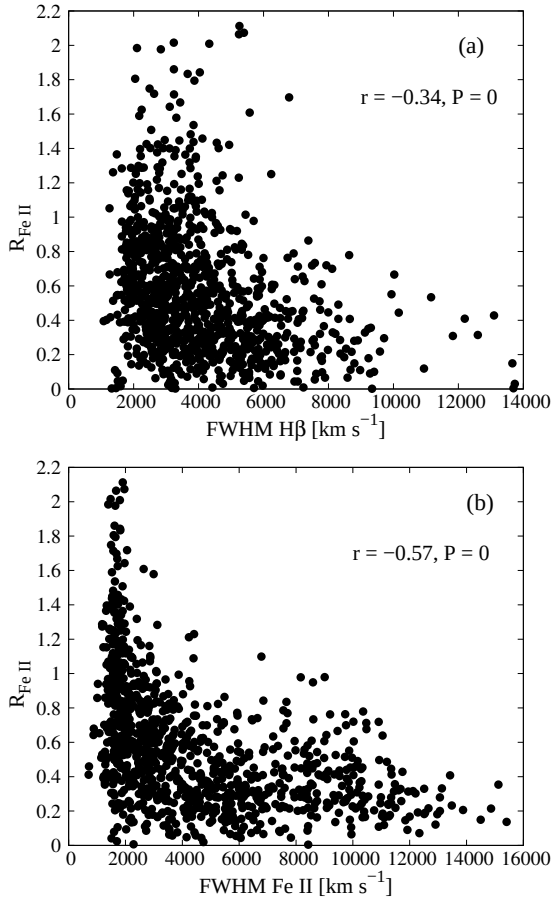

Fig. 3. Relationship between FeII [4434-4684]/Hβ ratio (R_{FeII}) and FWHM Hβ (a) and FWHM Fe II (b). The Spearman coefficients of correlations (r) and P-values are given in graphs.

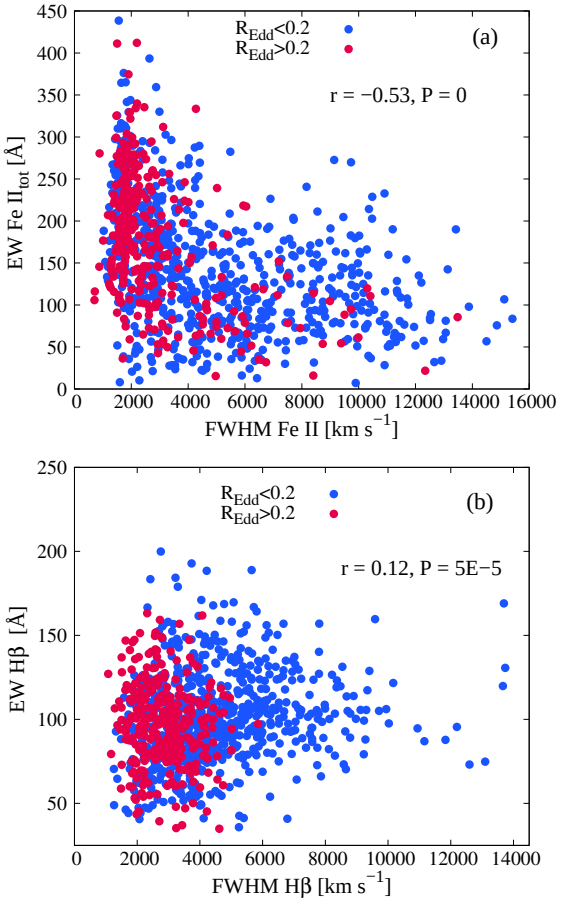

Fig. 4. Relationship between EW Fe II_{tot} and FWHM Fe II (a) and the same but for the EW Hβ and FWHM Hβ (b). The blue points denote objects with an Eddington ratio lower than 0.2, while red points indicate sources with an Eddington ratio larger than 0.2. The Spearman coefficients of correlations (r) and P-values are given in graphs.

tried to plot FWHM Fe II versus R_{FeII} ratio, instead standardly used FWHM Hβ. We found that anti-correlation between these parameters is sharper compared to the FWHM Hβ versus R_{FeII} anti-correlation. The anti-correlation significantly increases and the Spearman coefficient of correlation becomes r = –0.57, P = 0 (see Figure 3(b), Table 1). Although the widths of Hβ and Fe II are highly correlated with each other (r = 0.66, P = 0), it seems that FWHM Fe II gives the better trace for the underlying physics of this anti-correlation.

Afterwards, we examined R_{FeII} parameter, which is complex, since it represents the ratio of fluxes of two lines, Fe II and Hβ. We checked what is relation between EWs of each of these two lines with their FWHMs (see Figure 4, Table 1). We found that EW Fe II_{tot} versus FWHM Fe II gives high anti-correlation (r = –0.53, P = 0), with very similar relationship between parameters as given in the quasar main sequence. On the other hand, EW Hβ versus FWHM Hβ shows no correlation. Since Eddington ratio (R_{Edd}) has been suggested as the driving mechanism of EV1 correlations, we investigated the role of R_{Edd} in relationships of the EW Fe II and EW Hβ with their widths. Since the value $R_{Edd} \sim 0.2$ is recognised in literature as possible critical value for which large changes occur in the accretion mode and structure of an AGN (Wang et al. 2014; Ganci et al. 2019), we plot dots in Figure 4 with different colours for R_{Edd} larger and smaller than 0.2. Results imply that objects with an R_{Edd} larger than 0.2 are mainly objects with EW Fe II_{tot} > 150 Å. We found no correlation between EW Hβ and R_{Edd}, while EW Fe II_{tot} has moderate correlation with R_{Edd} (r = 0.34, P = 0). As expected, the widths of both lines are in strong anti-correlation width R_{Edd}. The coefficient of correlation between R_{Edd} and FWHM Fe II is r = –0.51, P = 0, while for FWHM Hβ it is r = –0.60, P = 0.

We examined possible effects of mathematical coupling on the EW Fe II-FWHM Fe II anti-correlation, since both quantities refer to the same line. Assuming a Gaussian shape for the Fe II lines, these two parameters are related as EW Fe II = $F_{FeII}/F_{cont} \sim (A_{FeII}/F_{cont}) \cdot$ FWHM Fe II, where F_{FeII} and A_{FeII} are the flux and amplitude of the Fe II line, while F_{cont} is the flux of the continuum under the Fe II line. This implies that, if the ratio A_{FeII}/F_{cont} remains approximately constant across the sample, EW Fe II and FWHM Fe II would exhibit a positive linear relationship due to the mathematical coupling between these two quantities. As seen in the data, a weak positive trend is observed for EW Hβ versus FWHM Hβ, whereas EW Fe II versus FWHM Fe II relationship shows a strong negative, non-linear dependency, suggesting a physical origin (see Figure 4). This analysis implies that the simplified correlation underlying the quasar main sequence, which contains fewer parameters but represents the same physical background, is actually EW Fe II versus FWHM Fe II. This anti-correlation shows that as Eddington ratio increases, the Fe II lines become narrower and the EW Fe II grows. In further analysis, we focus to this anti-correlation in order to analyse it in more details.

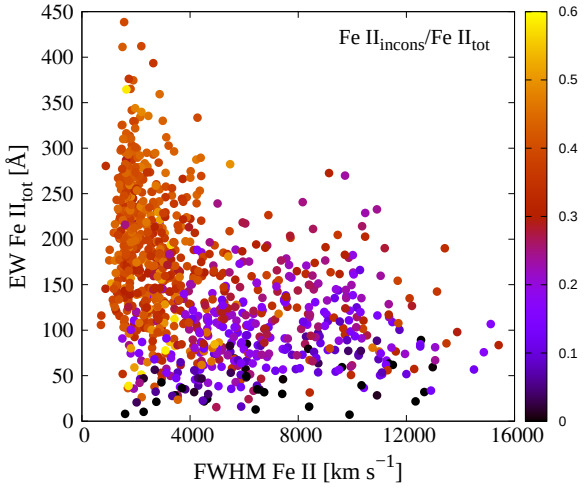

Fig. 5. Contribution of the Fe II$_{incons}$ lines to the total Fe II flux in the 4000–5600 Å range. Colours indicate the variation of the Fe II$_{incons}$/Fe II$_{tot}$ ratio across the EW Fe II$_{tot}$–FWHM Fe II parameter space.

3.2. Inconsistent Fe II lines in the contest of the quasar main sequence

We investigated the role of different groups of Fe II lines in the EW Fe II versus FWHM Fe II anti-correlation, and consequently in the quasar main sequence. First, we focused to the Fe II$_{incons}$ lines, due to their specific behaviour in the spectra. It is found that for objects with low Eddington ratio and broad Fe II lines, Fe II$_{incons}$ are weak or absent, as it is expected following their low transition probabilities. However, as Eddington ratio increases and line widths decrease, the intensity of these lines grows relative to Fe II$_{cons}$ lines, and they become surprisingly strong, in some cases exceeding expected values by up to two orders of magnitude (Kovačević-Dojčinović et al. 2025).

In Figure 5 we plotted EW Fe II$_{tot}$ versus FWHM Fe II anti-correlation, coloured by contribution of Fe II$_{incons}$ in the total Fe II flux in the 4000–5600 Å range. It could be seen that percentage of their contribution in total Fe II flux grows for the objects with large EW Fe II$_{tot}$, which have narrower Fe II lines. For objects with EW Fe II$_{tot}$ > 150 Å and FWHM Fe II < 5000 km s^{-1}, the contribution of the Fe II$_{incons}$ makes up from 30% to 50% of the total Fe II flux (see red and orange dots in Figure 5). On the other hand, for objects with smaller EW Fe II$_{tot}$ and generally broader widths, the contribution of the Fe II$_{incons}$ is mainly up to 20% (blue and black dots in Figure 5).

These results implies that inconsistent Fe II lines have important role in the growth of the total Fe II flux for narrower Fe II lines. Therefore we investigated separately the correlations of consistent and inconsistent Fe II lines with the Fe II width. We found that EW Fe II$_{incons}$ lines are in significantly stronger anti-correlation with Fe II width, than EW Fe II$_{cons}$ (see Figure 6). By using only the EW of Fe II$_{incons}$ lines in 4000–5600 Å range, we found that the anti-correlation with FWHM Fe II becomes stronger than for total Fe II, with coefficient of correlation r = –0.64, P = 0 (see Figure 6a). On the other hand, when using only the EW of consistent Fe II lines, this anti-correlation is lower than for total Fe II, and it becomes r = –0.38, P = 0 (see Figure 6b). The EW Fe II$_{incons}$ are also in stronger anti-correlation with FWHM Hβ than EW Fe II$_{cons}$, and in significantly stronger correlation with R$_{Edd}$ (see Table 1).

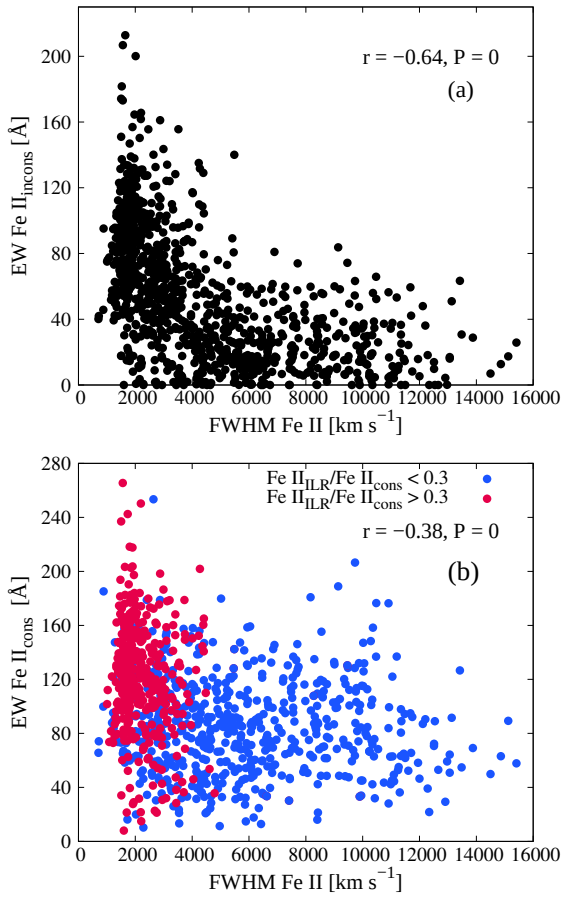

Fig. 6. Correlation between the FWHM of Fe II and the EW of Fe II$_{incons}$ (a) and the EW of Fe II$_{cons}$ (b). In panel (b), blue points denote objects in which the ILR component contributes less than 30% of the Fe II$_{cons}$ flux, while red points mark sources with an ILR contribution exceeding 30% of the Fe II$_{cons}$ flux.

In order to additionally analyse and quantify the changes of different spectral parameters for spectra with narrower Fe II, we calculated the mean values for various spectral parameters in different Fe II width ranges (see Table 2). In the last column of the table we gave the ratios between the mean parameter values for subsets with the broadest and with the narrowest Fe II widths (FWHM Fe II > 6000 km s^{-1} and FWHM Fe II < 2000 km s^{-1}, respectively). We found that all mean parameters related to the Fe II flux increase rapidly for subsets with narrower Fe II, while the mean EW Hβ shows a slight decrease. The mean value of R$_{FeII}$ increases by a factor of 3.5, EW Fe II$_{tot}$ by a factor of 2, EW Fe II$_{cons}$ increases 1.5 times, while the mean value of the EW Fe II$_{incons}$ shows the largest increase, by a factor of 3.6. The mean contribution of Fe II$_{incons}$ in total Fe II flux is doubled in the subset with narrowest Fe II comparing the subset with the broadest Fe II lines. The Fe II$_{incons}$ in average make for 40% of total Fe II flux for subset with FWHM Fe II < 2000 km s^{-1}. The observed trends remain significant when the estimated 1σ uncertainties in flux and EW of the various Fe II components are taken into account. These results imply that although both consistent and inconsistent Fe II lines grow for narrower spectra and higher R$_{Edd}$, the inconsistent Fe II lines exhibit a more pronounced growth than the consistent ones.

Table 1. Correlations between different properties of Fe II and Hβ lines and some physical parameters.

		FWHM Fe II	FWHM Hβ	logR_{Edd}
R_{FeII}	r	–0.57	–0.34	0.33
	P	0	0	0
Fe II_{tot}/Hβ	r	–0.56	–0.34	0.33
	P	0	0	0
FWHM Fe II	r	1	0.66	–0.51
	P	0	0	0
FWHM Hβ	r	0.66	1	–0.60
	P	0	0	0
EW Hβ	r	0.32	0.12	–0.12
	P	0	5E-5	1E-4
EW Fe II_{tot}	r	–0.53	–0.34	0.34
	P	0	0	0
EW Fe II_{cons}	r	–0.38	–0.22	0.27
	P	0	3E-13	0
EW Fe II_{incons}	r	–0.64	–0.43	0.40
	P	0	0	0

Notes. Table contains Spearman coefficients of correlation (r) and P-values.

3.3. Consistent Fe II lines: Growth of the ILR contribution

In our Fe II model, the consistent Fe II lines with estimated FWHM smaller than 5000 km s^{-1}, are fitted with two-components, ILR and VBLR, while for broader spectra we assume that Fe II lines have only VBLR component. We tested the role of the Fe II_{ILR} and Fe II_{VBLR} components in growth of the Fe II_{cons}, in context of the quasar main sequence. In Figure 6 b, the objects are coloured in different colours according to the Fe II_{ILR} flux contribution in Fe II_{cons} flux. We found that objects with a Fe II_{ILR} flux contribution larger than 30% dominate within the objects with a narrower FWHM Fe II and at the same time with a large EW Fe II_{cons}.

The growth of the EW Fe II_{ILR} for objects with smaller Fe II widths could also be seen in Table 2, for subsets where Fe II is modelled with both components (FWHM Fe II < 5000 km s^{-1}). The mean value of EW Fe II_{ILR} in the subset with FWHM Fe II < 2000 km s^{-1} is higher by a factor of 1.44 than in the subset with Fe II line widths within the range 2000–4000 km s^{-1}. Contrary of the Fe II ILR component, there are no significant changes in the mean value of the EW Fe II_{VBLR} for subsets with different Fe II widths. It seems that growth of the EW Fe II_{cons} for objects with narrower Fe II lines is dominantly caused by growth of the ILR components, while EWs of VBLR components in average remains the same. The Fe II ILR components in average make for 38% of Fe II_{cons} flux for subset with FWHM Fe II < 2000 km s^{-1}, while for subsets with broader Fe II lines their contribution decreases.

We additionally examined the role of the Fe II ILR components in growth of the total Fe II emission by performing one test. Following the distribution of parameters in EW Fe II_{tot} versus FWHM Fe II plane (see Fig. 5), we selected two subsets with different properties, belonging to the two ends of this distribution. The first subset are the objects with the strongest Fe II lines, selected to have EW Fe II_{tot} > 150 Å and FWHM Fe II < 5000 km s^{-1} (418 objects). The second subset are the spectra with weak and very broad Fe II lines, selected to have FWHM Fe II > 5000 km s^{-1} (338 objects). We re-binned all spectra, and normalised them to have the same continuum intensity at 5630 Å, which is the only one adopted continuum window in fitting procedure. Afterwards, we found the mean spectrum for each subset, and we fit these two mean spectra with our model. In narrower mean spectrum, the Fe II_{cons} lines are fitted with the two-component model, while in the broad mean spectrum they are fitted with single-component model, assuming that they have only the Fe II VBLR component. The best fits of the two mean spectra are shown in Fig. 7, where Fe II_{incons}, Fe II_{ILR} and Fe II_{VBLR} components are shaded with different colours. We found that inconsistent Fe II lines are strong in the mean spectrum with strong and narrow Fe II (Fig. 7, Panel A), while they are negligible in the broad line mean spectrum (Fig. 7, Panel B), where only Fe II_{VBLR} contributes to the total Fe II emission.

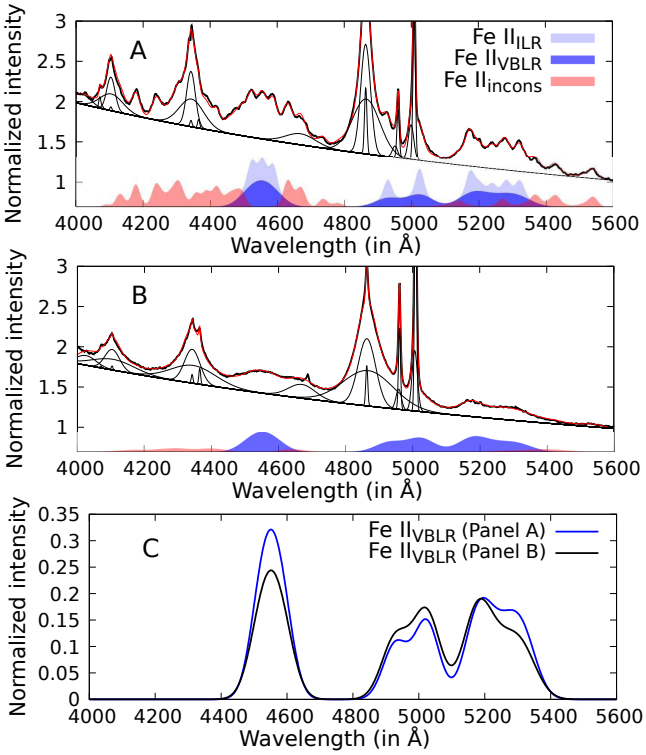

Fig. 7. Decomposition of Fe II lines in two mean spectra. Panel A: Mean spectrum obtained from the subset with EW Fe II_{tot} > 150 Å and FWHM Fe II < 5000 km s^{-1}. Panel B: Mean spectrum obtained from the subset with FWHM Fe II > 5000 km s^{-1}. The consistent Fe II lines are shaded with the blue colour, where the sum of the ILR components is shaded with the light-blue, and the sum of the VBLR components with the dark-blue. The inconsistent Fe II lines are shaded with the red colour. In both panels, the best fit is denoted with the red line. The Fe II_{VBLR} components obtained from the best fit of the mean spectra are compared in Panel C.

However, most interestingly, the Fe II VBLR component of the mean spectrum made from the subset with EW Fe II_{tot} > 150 Å and FWHM Fe II < 5000 km s^{-1}, is very similar to the Fe II VBLR component of the mean spectrum from the FWHM Fe II > 5000 km s^{-1} subset (see Fig. 7, Panel C). The width of the Fe II VBLR component in narrow mean spectrum is ~5400 km s^{-1}, and in broad one is ~5900 km s^{-1}, while both EWs are ~100 Å. These results additionally illustrate that the very strong EW Fe II in some objects is dominantly caused by the enhanced emission of the EW Fe II_{incons} and EW Fe II_{ILR}, while the EW Fe II_{VBLR} on average remains the same in the entire sample.

Table 2. Mean values of the measured parameters for different FWHM Fe II ranges.

(1)	(2)	(3)	(4)	(5)	(6)
Width range	FWHM FeII>6000 [255]	4000<FWHM FeII<6000 [175]	2000<FWHM FeII<4000 [327]	FWHM FeII<2000 [256]	$\frac{(5)}{(2)}$
FWHM Fe II	8969 ± 2201	4901 ± 603	2827 ± 524	1648 ± 234	0.18
FWHM Hβ	5778 ± 1965	4023 ± 1311	3463 ± 1155	2746 ± 930	0.47
R_{FeII}	0.36 ± 0.19	0.41 ± 0.23	0.59 ± 0.29	0.91 ± 0.43	2.53
EW Fe II_{tot}	108 ± 49	119 ± 61	167 ± 78	215 ± 84	2.00
EW Fe II_{cons}	84 ± 34	85 ± 37	103 ± 47	129 ± 49	1.54
EW $FeII_{incons}$	24 ± 18	34 ± 29	65 ± 35	87 ± 37	3.62
Fe II_{incons}/Fe II_{tot}	0.20 ± 0.11	0.26 ± 0.12	0.37 ± 0.10	0.40 ± 0.06	2.00
EW Fe II_{ILR}	–	7 ± 23	34 ± 26	49 ± 24	–
EW Fe II_{VBLR}	82 ± 35	77 ± 34	69 ± 37	80 ± 32	0.98
Fe II_{ILR}/Fe II_{cons}	–	0.06 ± 0.18	0.31 ± 0.21	0.38 ± 0.13	–
EW Hβ	110 ± 26	102 ± 25	101 ± 29	88 ± 36	0.80
R_{Edd}	0.09 ± 0.08	0.13 ± 0.12	0.20 ± 0.16	0.30 ± 0.25	3.33

Notes. Table contains mean values ± standard deviation. The number of objects in each FWHM Fe II range is given in brackets. The FWHMs of lines are given in km s^{-1}, and EWs are given in Å. Column (6) gives the ratios between the mean values obtained for the subsets with the narrowest and with the broadest Fe II widths (columns 5 and 2).

3.4. Fe II lines: A signature of the AGN dichotomy

As previously noted in Section 1, it has been observed that R_{FeII} versus FWHM Hβ anti-correlation can be utilised for classification purposes (Sulentic et al. 2000a; Marziani et al. 2001). Sulentic et al. (2000a) suggested that the specific shape of this anti-correlation, with two visually distinct parameter branches in the R_{FeII} versus FWHM Hβ plane, reveals a division into two AGN populations. These two populations are visually separated at FWHM Hβ = 4000 km s^{-1}, where Population A has FWHM Hβ < 4000 km s^{-1} and Population B, FWHM Hβ > 4000 km s^{-1}. The comparison of different spectral properties in radio, optical, UV and X-range among these two populations, indicated significant differences among these two groups of objects (Sulentic et al. 2011; Marziani et al. 2018).

We found that EW Fe II versus FWHM Fe II anti-correlation has higher coefficient of correlation comparing R_{FeII} versus FWHM Hβ, implying that it is probably more fundamental. Therefore, we investigated whether it also could reflect the AGN dichotomy. The results presented in Fig. 4a, Fig. 5 and Fig. 6b reveal that the EW Fe II versus FWHM Fe II correlation space indicate two branches of the data. One branch is with FWHM Fe II < 5000 km s^{-1} and strong EW Fe II (>150 Å), which is distinguished with higher Eddington ratio, and higher contribution of the Fe II_{incons} and Fe II_{ILR} in Fe II_{tot} flux. As it could be seen in Table 2, the growth of the EW Fe II_{tot} in this group is mainly caused by the growth of EW Fe II_{incons} and EW Fe II_{ILR}. The other branch in EW Fe II versus FWHM Fe II plane represents the objects with smaller R_{Edd} and smaller contribution of the Fe II_{incons} and Fe II_{ILR} in total EW Fe II. In these objects, EW Fe II_{tot} mainly consists of EW Fe II_{VBLR}, and it goes up to ~150 Å with average value of ~100 Å. This group mostly includes the objects with broad FWHM Fe II (>5000 km s^{-1}), weak EW Fe II_{tot} and low Eddington ratio. At the breaking point of these two branches of the data are objects with FWHM Fe II < 5000 km s^{-1} and weak EW Fe II (<150 Å), which represents a mixture of these two groups.

It seems that those two groups of objects are even more clearly separated in FWHM Fe II versus $\log\lambda L_{5100}$ parameter space (see Fig. 8), where they are positioned in two visually distinct branches with different dependencies between FWHM Fe II and luminosity, forming a heart-like shape. The objects with contribution of the sum of Fe II_{incons} and Fe II_{ILR} larger than ~40% in the total Fe II flux are concentrated in the left branch and have steeper FWHM Fe II versus $\log\lambda L_{5100}$ relationship. As expected, these objects generally exhibit higher Eddington ratios than those distributed along the right branch of the diagram. Most sources with Eddington ratios exceeding the critical value of R_{Edd} ~ 0.2 are located on the left branch (see Figure 8b).

We investigated whether objects populating the two branches of the heart-shaped diagram differ in their spectral properties and global parameters, and compared these trends with those found for the Pop A/Pop B dichotomy. It has been found that Population A sources generally have lower black hole masses and enhanced outflow signatures relative to Population B sources (Marziani et al. 2018; Shen & Ho 2014). Also, it has been suggested that orientation effects may contribute to the dispersion in FWHM Hβ along the quasar main sequence at fixed R_{FeII} (Shen & Ho 2014). In contrast to the Pop A/Pop B division, we found no difference in the M_{BH} distributions for objects in two branches of FWHM Fe II versus $\log\lambda L_{5100}$ diagram. We examined the possible presence of AGN-driven outflows by analysing the complex profile of the [O III] 5007 Å line, which is known to be a good indicator of outflow presence and strength (see e.g. Woo et al. 2016; Rakshit & Woo 2018). We used the velocity shift of the [O III] 5007 Å wing component to trace the outflow contribution. The results show that [O III] wing components are more blueshifted in the left branch of the heart-shaped diagram indicating the outflow presence. The details of analysis and plot are given in Appendix B, Figure B.1. Shen & Ho (2014) used the ratio of the FWHM Hβ and the second moment of the emission-line profile of the same line (σ Hβ) as one of the indicators of the orientation effects. The variation of this

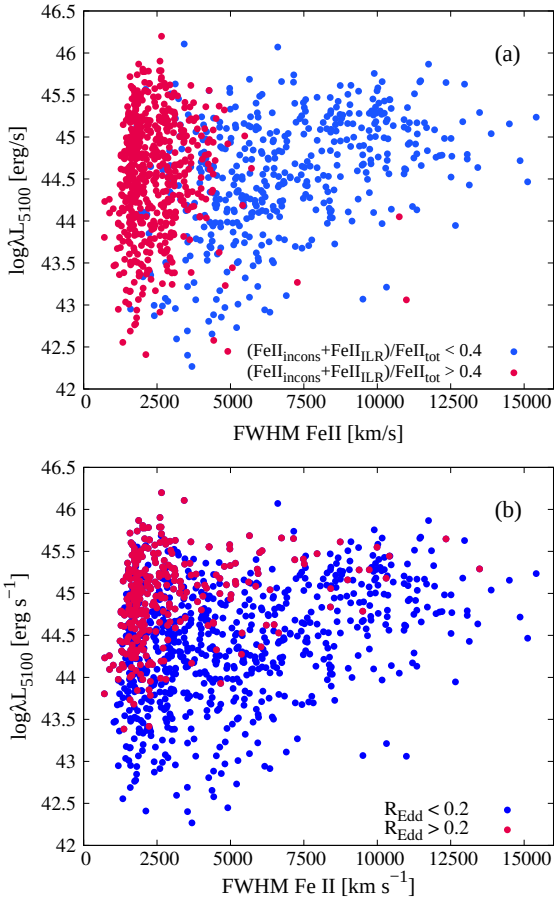

Fig. 8. Relationship between logλL_{5100} and the width of the Fe II lines. In panel (a), red points mark objects in which the combined contribution of Fe II$_{incons}$ and Fe II$_{ILR}$ exceeds 40 % of the total Fe II flux, whereas blue points denote sources in which this contribution falls below the same threshold. The distribution of objects with R$_{Edd}$ smaller and larger than 0.2 is shown in panel (b).

ratio traces changes in the Hβ profile, which is known to differ systematically between Population A and Population B sources (Marziani et al. 2018). Shen & Ho (2014) suppose that in the case of the disc-like BLR geometry, σ Hβ is less affected by inclination effects leading to a larger FWHM Hβ/σ Hβ ratio as inclination increases. We computed this ratio for our sample and found that it follows the dichotomy of the heart-shaped diagram, where sources with lower FWHM Hβ /σ Hβ values are predominantly located in the left branch (see Appendix B, Figure B.2), indicating smaller inclinations for these objects. However, these variations in Hβ profile, which distinguish Pop A and Pop B sources, as well as objects in two branches of the FWHM Fe II versus log λL_{5100} diagram, may also arise from factors other than inclination, such as structural differences in the accretion disc or the BLR (Collin et al. 2006).

Additionally, we focus on the well known anti-correlation between EW Fe II and EW [O III], which is part of EV1 correlations found by Boroson & Green (1992), and we tried to analyse it from an another angle. In Figure 9 we coloured two relationships, EW Fe II versus FWHM Fe II and logλL_{5100} versus FWHM Fe II, with different colours according to the value of the [O III]$_{5007Å}$/ Hβ_{NLR} ratio. This ratio could be considered as an indicator of the shape of the ionisation continuum (Baldwin et al. 1981) in the region where narrow lines arise. We found that objects with narrow and strong EW Fe II, which are also the objects in the left branch of the logλL_{5100} versus FWHM Fe II diagram, mostly have smaller [O III]/Hβ_{NLR} ratio, comparing the rest of the objects (see Figure 9). For the narrowest and strongest Fe II, this ratio becomes even log([O III]/Hβ_{NLR}) < 0.5. Some of these objects correspond to NLSy1 galaxies, which are defined as having ([O III]$_{5007}$/Hβ_{NLR}) < 3 and FWHM Hβ < 2000 km s^{-1} (Osterbrock & Pogge 1985; Goodrich 1989). In our sample, there are 22 objects with these properties and they are located in the left branch of the diagram, between the sources with the narrowest Fe II line widths (~1500 km s^{-1}) and with logλL_{5100} up to 44.5 erg s^{-1}.

Finally, we compared the dichotomy seen in the heart-shaped diagram with classical division into Pop A/Pop B (see Fig. 10). We find that the left and right branches of the diagram approximately follow the Pop A/Pop B classification. Pop A sources are mostly located in the left branch, Pop B in the right one, while in the FWHM Fe II range between 4000–6000 km s^{-1}, there is a mixture of Pop A and Pop B sources.

4. Discussion

4.1. Dissecting the R_{FeII} parameter

The principal component analysis performed by Boroson & Green (1992) revealed that the parameter R$_{FeII}$ is governed by Eddington ratio. Since then, the parameter R$_{FeII}$ has been widely discussed in the literature in the context of its significant relationship with Eddington ratio and accretion rate, although the nature of this relationship is not yet understood (see e.g. Sulentic et al. 2000a; Boroson 2002; Shen & Ho 2014; Yu et al. 2020; Marziani et al. 2025). It is proposed that R$_{FeII}$ could be used for improving the accuracy of the M$_{BH}$ estimation (Du & Wang 2019; Yu et al. 2020). Namely, it is found that objects with high Eddington ratio deviate from the empirical R$_{BLR}$–L$_{5100}$ relationship found in Kaspi et al. (2000) and used for M$_{BH}$ estimation (see Peterson et al. 2004). Since R$_{FeII}$ was found to correlate with that deviation, it is proposed to use the parameter R$_{FeII}$ to improve the R$_{BLR}$–L$_{5100}$ relationship (Du & Wang 2019; Yu et al. 2020). On the other hand, Marziani & Sulentic (2014) proposed the parameter R$_{FeII}$ as an indicator of objects with highest value of Eddington ratio, defined as extreme Population A sources, with R$_{FeII}$ > 1. These objects are characterised by a number of specific properties that distinguish them from other objects in the AGN population (see Marziani et al. 2025).

In order to better understand the nature of the relationship between R$_{FeII}$ and R$_{Edd}$, and the role of the Eddington ratio in quasar main sequence correlation, we applied the flexible and complex Fe II model, which enabled us to precisely measure the width of the Fe II lines and to follow the changes among the relative intensities of different Fe II line groups along the quasar main sequence. Our results imply that a simpler and more fundamental relationship underlying the anti-correlation of R$_{FeII}$ versus FWHM Hβ may be the EW Fe II versus FWHM Fe II, where EW Fe II becomes even twice as strong in AGNs with narrow Fe II lines and high Eddington ratio, compared to those with low Eddington ratio. Since there is no significant correlation between EW Hβ and Eddington ratio, this implies that the EW Fe II parameter is itself an indicator of the R$_{Edd}$ growth. This raises the question of why EW Fe II may represent a more direct physical link to R$_{Edd}$ than EW Hβ. This may be related to the exceptionally complex atomic structure of Fe II, characterised by a very large number of closely spaced energy levels and, consequently, numerous possible transitions. This property makes

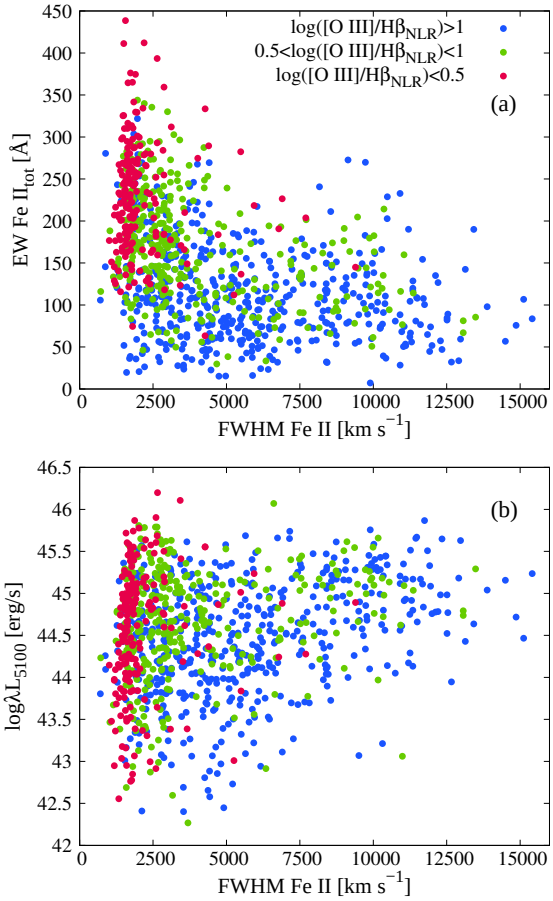

Fig. 9. Variation of the [O III]/Hβ_{NLR} ratio across the FWHM Fe II–EW Fe II$_{tot}$ (a) and FWHM Fe II–logλL_{5100} (b) parameter space. The different colours of the points indicate the strength of the log[O III]/Hβ_{NLR} ratio.

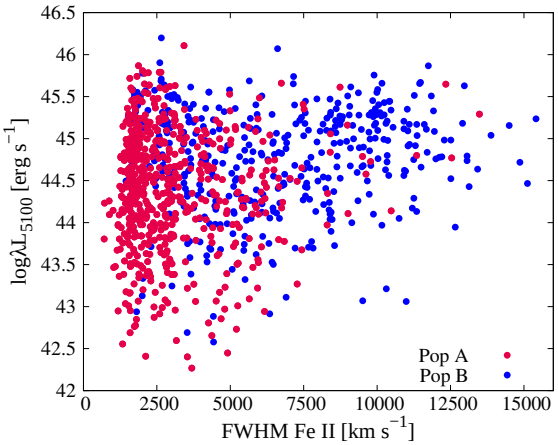

Fig. 10. Distribution of the Pop A and Pop B objects in the FWHM Fe II versus log λL_{5100} plane.

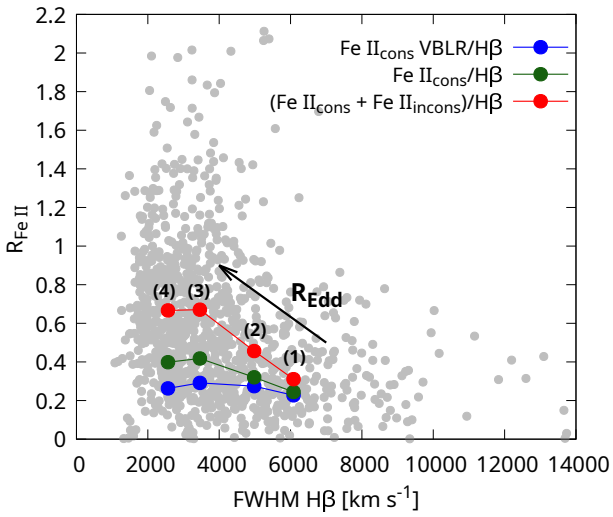

Fig. 11. Growth of different Fe II components in the quasar main sequence. The sample is divided into four subsets according to R_{Edd}: (1) $R_{Edd} < 0.03$ (71 objects), (2) $0.03 < R_{Edd} < 0.1$ (325 objects), (3) $0.1 < R_{Edd} < 0.3$ (471 objects), and (4) $R_{Edd} > 0.3$ (154 objects). For each subset, we found the mean ratio of different Fe II components in 4434–4684 Å range and broad Hβ (marked with different colours), as well as the mean of the FWHM Hβ. The mean values of each subset are indicated by the corresponding numbers (1–4) on the top and plotted over the quasar main sequence.

Fe II distinct from other atomic species and enables a wide variety of atomic processes that can be triggered under specific astrophysical conditions. At the same time, an increase in R_{Edd} may significantly modify the physical conditions and structure of the BLR. Such changes could activate additional atomic processes in Fe II or enhance the efficiency of existing ones, leading to additional iron emission.

Based on the shape of the quasar main sequence, it could be seen that a small FWHM Hβ (and thus a small FWHM Fe II) appears to be a necessary, but not sufficient condition for a high R_{FeII} value. In the FWHM Fe II versus EW Fe II parameter space, the objects with an EW Fe II less than ~150 Å are uniformly present for all widths of the Fe II lines, while the strong Fe II emitters (EW Fe II larger than ~150 Å) appear only for objects with narrower lines (FWHM Fe II < 5000 km s^{-1}), followed with a high Eddington ratio.

We separately analysed the behaviour of the EW Fe II$_{incons}$ and EW Fe II$_{cons}$ along the main sequence, and additionally, within the EW Fe II$_{cons}$, we analysed the changes in their line components, EW Fe II$_{ILR}$ and EW Fe II$_{VBLR}$. We found that the EW Fe II$_{VBLR}$ components remain on average unchanged along the quasar main sequence, while the EW Fe II$_{incons}$ and EW Fe II$_{ILR}$ increase for smaller line widths (see Figure 7 and Table 2), and high Eddington ratio. This is additionally demonstrated in Figure 11, where the sample is divided into different subsets according to the R_{Edd}, from subset with the smallest R_{Edd} (assigned as (1) on the plot) to the subset with the largest R_{Edd} (assigned as (4) on the plot). The blue dots represent the mean values of the Fe II$_{VBLR}$/Hβ ratio, the green dots are the mean values of Fe II$_{cons}$/Hβ (where both components are included, ILR+VBLR). Finally, when we included Fe II$_{incons}$, we obtained the red dots, which represent the mean values of R_{FeII}, i.e. the ratio of total Fe II in the range 4434–4684 Å (Fe II$_{cons}$ + Fe II$_{incons}$) divided by Hβ. It could be seen that the mean values of the EW Fe II$_{VBLR}$ do not change much for different R_{Edd} (blue dots), while EW Fe II$_{ILR}$ slightly increases for higher R_{Edd} (green dots). However, the largest increase is in the EW Fe II$_{incons}$ lines (red dots), which cause the mean value of the R_{FeII} to almost double from the subset (1) with low R_{Edd}, to the subset (4) with high R_{Edd}.

The narrow width of Fe II and Hβ lines, observed in extreme Fe II emitters, may be due to various physical causes, or due to a

combination of some of them. It is most often explained by low black hole mass or by low inclination (see e.g. Marziani et al. 2001; Shen & Ho 2014; Sun & Shen 2015). In general, the widths of Fe II and Hβ can be influenced by certain other factors as well, as emission region stratification, where dominant emission originates from regions further from the black hole, or by some atomic processes which could produce line narrowing. Our results imply that the increase of the R_{FeII} for objects with smaller line widths, is actually caused by increase in the flux of inconsistent Fe II lines and Fe II$_{ILR}$ components, which are both present in 4434–4684 Å range (see Figure 1). Since ILR components are narrower than VBLR, their larger contribution in total Fe II flux, leads to narrowing of the profile of Fe II lines, i.e. to decreasing of the FWHM Fe II. Similarly, the relationship between the R_{FeII} parameter and R_{Edd} is actually caused by the relationship of the EW Fe II$_{ILR}$, and specially the EW Fe II$_{incons}$ with R_{Edd} (Figure 11). The question is why the additional Fe II component (ILR) appears in objects with high Eddington ratio, and in particular, why inconsistent Fe II lines, which flux should be very weak or negligible according to their transition probabilities, become very strong in these objects.

It is possible that for high Eddington ratio, the additional processes could be activated in the other emission region than one where Fe II$_{VBLR}$ component arise, which may results with efficient emission of Fe II$_{ILR}$ and Fe II$_{incons}$ lines. Indeed, theoretical considerations of the changes that occur in AGNs with increasing R_{Edd} have estimated that a fundamental change in accretion mode and BLR structure occurs for a critical value of R_{Edd} in the interval 0.1–0.3 (Wang et al. 2014; Ganci et al. 2019). In Figure 11, it could be seen that the highest growth of R_{FeII} is happening for objects with $R_{Edd} > 0.1$, which belong to the subsets (3) and (4). This may indicate that fundamental changes in accretion could lead to modifications in the BLR structure and its stratification, as well as to the activation of new processes of Fe II emission in different layers of the BLR, which would result in the growth of additional Fe II components and thus an increase in the total Fe II emission.

4.2. Complexity of the physical processes behind strong Fe II emission

Conventional photoionisation models estimate Fe IIλ 4570 Å/Hβ to be typically 0.2 (Kwan & Krolik 1981), which is satisfied in the case of objects with weak Fe II lines. In order to theoretically explain the spectra with a significant enhancement in Fe II emission, the other excitation processes were taken into account, such as collisional excitation, line trapping (see Joly 1987; Baldwin et al. 2004), pumping the Fe II emission by Lyα fluorescence (Marinello et al. 2020), or non-radiative heating due to shocks and outflows (Collin & Joly 2000). It appears that the processes and physical conditions under which extreme Fe II emission occurs are still not well understood. Inclusion of a large number of different atomic processes and data in spectral synthesis code CLOUDY was not sufficient for the theoretical reproduction of the optical Fe II flux and relative intensities among the Fe II lines in the case of extremely strong Fe II emitters (Zhang et al. 2024; Pandey et al. 2025). It is suggested that super-solar metallicity in the BLR is required to explain the extreme iron emission (Panda et al. 2019b). The problem of metallicity in AGN emission regions was dealt by a large number of authors (Hamann et al. 2002; Baldwin et al. 2003; Negrete et al. 2012). Gaskell et al. (2022) proposed that strong soft X-ray excess increases the iron abundance by orders of magnitude by destroying dust grains and releasing iron into

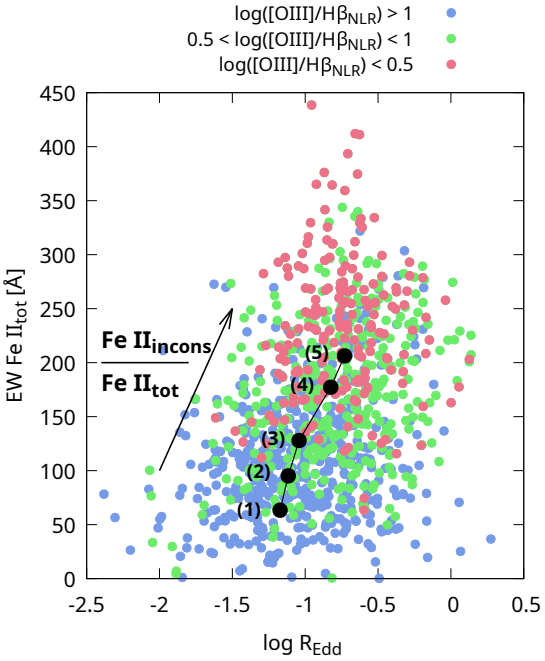

Fig. 12. Growth of the contribution of Fe II$_{incons}$ in total Fe II, with the increase of the R_{Edd} and decrease of the [O III]/Hβ_{NLR}. The sample is divided into five subsets according to the Fe II$_{incons}$/Fe II$_{tot}$ ratio: (1) Fe II$_{incons}$/Fe II$_{tot}$ < 0.1 (87 objects), (2) 0.1 < Fe II$_{incons}$/Fe II$_{tot}$ < 0.2 (134 objects), (3) 0.2 < Fe II$_{incons}$/Fe II$_{tot}$ < 0.3 (187 objects), (4) 0.3 < Fe II$_{incons}$/Fe II$_{tot}$ < 0.4 (320 objects), and (5) Fe II$_{incons}$/Fe II$_{tot}$ > 0.4 (293 objects). For each subset, we found the mean of EW Fe II$_{tot}$ and R_{Edd}, which are plotted with black dots and indicated by the corresponding numbers (1–5). Additionally, the points are coloured according to log([O III]/Hβ_{NLR}) strength.

the gas phase. Several studies estimated BLR metallicity of very strong Fe II emitters by measuring the flux ratios of some broad emission lines (Śniegowska et al. 2021; Garnica et al. 2022; Floris et al. 2024). As a result, they obtained a super-solar metallicity in the BLR, which reaches several tens of solar metallicity.

In order to explain the high metallicity of BLR required for modelling the extreme Fe II emission, it has been proposed that the high metallicity of such objects could be caused by nuclear or circumnuclear star formation activity, which might be associated with supermassive black hole phenomena in some phase of AGN evolution (see Lípari & Terlevich 2006; Marziani et al. 2025). In this scenario, the BLR is consistently enriched in metals by starburst regions that could be located within torus, or even within the high-density gas of the accretion disc (Wang et al. 2011, 2023; Fan & Wu 2023; Huang et al. 2023). However, these assumptions are not observationally confirmed since BLR cannot be resolved.

The question is whether the assumption of such a high metallicity is justified or whether the same observational properties could be explained in another way. Temple et al. (2021) found that the several broad emission-line ratios, commonly used in the literature as indicators of BLR metallicity, can be reproduced by a model in which the line emission originates from two kinematically distinct regions with different physical conditions, without requiring metallicities above solar. As pointed out by Wills et al. (1985), the large observed Fe II fluxes require either that iron is several times overabundant (compared to solar ratios) or that some unknown process dominates the Fe II excitation. Here we consider whether the extremely strong Fe II emission can be

explained by the activation of additional atomic processes in certain part of Fe II emission region.

Following the Einstein coefficients for spontaneous emission, the optical Fe II emission is expected to be several orders of magnitude smaller than UV Fe II, but they are of the same order of magnitude in most of the AGN spectra (Joly 1981). The growth of the optical Fe II lines relative the UV Fe II is specially emphasised in strong Fe II emitters, located at the extreme end of quasar main sequence with $R_{FeII} > 1$. It is proposed that mechanism of self-absorption of the UV Fe II lines is responsible for this effect, causing the resonantly pumping the optical Fe II transitions, and therefore their significant increase in AGN spectra (Netzer 1980; Joly 1981; Collin & Joly 2000). However, it seems that similar process is happening among the optical Fe II lines themselves. The Fe II_{incons} lines should be up to two orders of magnitude smaller than Fe II_{cons}, and therefore they are expected to be very weak in spectra, even when Fe II_{cons} are strong. Since they are of the same order of magnitude as Fe II_{cons} in strong Fe II emitters, Kovačević-Dojčinović et al. (2025) proposed that the same mechanism of the self-absorption (radiation trapping) is responsible to transmission of energy from Fe II_{cons} to Fe II_{incons} lines. This effect is possible due to the specific configuration of the energy levels of the Fe II ions. Namely, the UV Fe II emission lines at ∼2800 Å have the same upper energy level as optical Fe II emission lines (both, consistent and inconsistent). At the same time, the lower levels of transitions of UV Fe II and optical consistent and inconsistent Fe II lines are all metastabiles (see Grotrian diagram in Figure 12, given in Kovačević-Dojčinović et al. (2025)), which is one of the main reasons for the transfer of energy of radiation first from the UV Fe II to the optical Fe II_{cons} lines, and then within optical lines from Fe II_{cons} to Fe II_{incons} lines. Moreover, it is found that both processes are related with growth of the R_{Edd}, where it is supposed that a high R_{Edd} causes an increase in the optical depth in the Fe II lines, which makes the self-absorption process more efficient (Kovačević-Dojčinović et al. 2025).

However, the transmission of energy caused by self-absorption, does not generally explain why, in extreme cases, up to 50% of the total radiative output from the BLR is released through Fe II emission (Joly 1981). The observed enhancement of iron emission could be attributed to the formation of localised emission regions within the complex AGN structure, where physical conditions could be suitable for activation of some additional excitation processes. Generally, strong line emission requires efficient population of the upper levels and at the same time efficient depopulation of the lower levels. The efficient population of the upper levels can be achieved by radiative or collisional excitation. For efficient radiative excitation, the shape of the continuum plays an important role, and for efficient collisional excitation, electrons of appropriate kinetic energy are required.

The strong Eddington ratio is related with appearance of an outflow, which is found to be present in spectra with strong and narrow optical Fe II lines (Shen & Ho 2014). The strong outflow may cause an effective collisional excitation, which leads to the more efficient population of the upper transition levels of UV and optical Fe II and at the same time depopulation of their lower metastable levels.

Our findings suggest that for objects with the strongest Fe II, the log([O III]/Hβ_{NLR}) is less than 0.5 (see Figure 9), which according to BPT diagram, implies classification into starburst galaxies, LINERs or composite objects (AGN+starburst) (see Kauffmann et al. 2003). Although this result indicates the possible presence of starburst regions in the NLR, their potential presence closer to the BLR could lead to more efficient collisional excitation and increased gas density, due to shock waves generated by supernova explosions (Lípari & Terlevich 2006), which would lead to enhanced Fe II emission.

On the other hand, a spectral energy distribution exhibiting enhanced flux at the energies required for ionisation and excitation of iron would make the photoexcitation of Fe II ions more efficient. The ionisation and excitation energies for optical Fe II are relatively low (7.9 eV and ∼5 eV, respectively), and their sum in units of wavelength corresponds to ∼960 Å. Therefore, the softer spectral energy distribution, with strong radiation in far-UV would contribute to a more efficient excitation of the upper levels of the optical Fe II lines. Indeed, several theoretical models of spectral energy distribution predict a softening of the ionising continuum and more luminous far-UV continuum for the sources with high Eddington ratio ($R_{Edd} > 0.1$), compared to those with lower Eddington ratio (Kubota & Done 2018; Ferland et al. 2020; Garnica et al. 2025). Moreover, the observed variation of the [O III]/Hβ_{NLR} ratio along the quasar main sequence (Figure 9) can be interpreted as a change in the shape of the ionising continuum within the NLR (Baldwin et al. 1981). The formation of [O III] ion requires an energy of 48.7 eV (the sum of the first and second ionisation energies), while a total energy of 12.7 eV is required to excite the upper level of the Hβ transition. The low ratio of the [O III]/Hβ_{NLR} in strong Fe II emitters indicates that in NLR of these objects, the excited Hβ atoms are more likely to be formed than double ionised [O III] ions, which require higher energies. If we assume that the shape of the ionising continuum in BLR is similar as the ionising continuum in NLR, it could imply presence of a softer ionising continuum in BLR of strong Fe II emitters, comparing to weak Fe II emitters, which would be very favourable for the excitation of the upper levels of the considered optical Fe II lines. This assumption is observationally supported since in the spectra of strong Fe II emitters, the lines of the helium ion (such as He II 4686 Å) tend to be smaller relative to the Fe II lines compared to those in weaker Fe II sources. Note that energy of helium ionisation is 24.6 eV, and energy of excitation of He II 4686 Å from the ground state is 51 eV.

However, the decrease in the [O III]/Hβ_{NLR} ratio may also be caused by other physical conditions. An increase in the electron density of the NLR towards the critical density of [O III] ($\sim 10^5$ cm^{-3}) would lead to more efficient collisional de-excitation, suppressing the [O III] emission and consequently decreasing the [O III]/Hβ_{NLR} ratio (Osterbrock & Ferland 2006; Wolf et al. 2026). Another possible explanation is the weakening of [O III] due to the so-called disappearing NLR in high-luminosity sources (Netzer et al. 2004). In addition, there are indications that metallicity may also affect the [O III]/Hβ_{NLR} ratio (Dopita et al. 2006; Feltre et al. 2016).

In Figure 12 we summarised the mentioned properties of optical Fe II emission. It could be seen that total Fe II emission grows as contribution of the Fe II_{incons} grows in total Fe II flux, which is related with increase of R_{Edd} and decrease of [O III]/Hβ_{NLR} ratio. Similarly as noticed for narrow line width, the high Eddington ratio is a necessary, but not a sufficient condition for very strong Fe II emission. On the other hand, the [O III]/Hβ_{NLR} ratio appears to be better indicator of extreme Fe II emitters, with low values of this ratio reflecting the particular physical conditions that characterise this subpopulation.

5. Conclusions

In this study, we have used a large sample of Type 1 AGN spectra to investigate the complex nature of the Fe II emission

region by analysing correlations between Fe II features and other spectral parameters. We focused in particular on the quasar main sequence anti-correlation to better understand the underlying physics, especially in the case of strong Fe II emitters. To achieve this, we applied a flexible and complex Fe II template that enabled us to decompose the Fe II emission in the optical range and to follow the behaviour of different groups of Fe II lines and their components along the quasar main sequence. The optical Fe II lines were divided into two large line groups, referred to as consistent and inconsistent, based on their transition probabilities. Furthermore, for the consistent Fe II lines, we applied a two-component model and separately examined the relative contributions from the ILR and the VBLR within the framework of the quasar main sequence. Summarising the main results, we outline the following conclusions:

1. The Fe II lines with widths below ~5000 km s^{-1} can be satisfactorily reproduced using a two-component model. In this model, the line wings are fitted with a broader Gaussian component associated with emission from the VBLR, while the line cores are fitted by a narrower Gaussian corresponding to emission from the ILR. The applied two-component Fe II model provides an improved accuracy in fitting Fe II lines in these objects. However, for sources exhibiting broader Fe II profiles (FWHM larger than ~5000 km s^{-1}), the model does not significantly enhance the fit quality, implying that in these objects the Fe II emission likely originates from a single kinematic region.
2. The anti-correlation between the EW Fe II and FWHM Fe II appears to represent a more fundamental relation underlying the quasar main sequence. Replacing the Hβ FWHM with the Fe II FWHM, obtained applying the complex Fe II template, significantly strengthens the quasar main sequence anti-correlation.
3. The increase in EW Fe II (and consequently in the parameter R_{FeII}) along the quasar main sequence is primarily caused by the enhancement of EW Fe II$_{incons}$ lines and, with a smaller contribution, by the enhancement of EW Fe II$_{ILR}$ components. The relative contribution of these components to the total Fe II flux increases with increasing Eddington ratio and decreasing Fe II line width. In contrast, the EW of Fe II$_{VBLR}$ components remain, on average, similar in both strong and weak Fe II emitters, exhibiting no significant variation along the quasar main sequence.
4. The strong Fe II emitters (EW Fe II > 150 Å) typically exhibit $R_{Edd} > 0.1$, FWHM Fe II < 5000 km s^{-1}, and log[O III]/Hβ_{NLR} < 1. In these objects, the Fe II$_{incons}$ and Fe II$_{ILR}$ components together contribute more than 50% of the total Fe II flux. However, small line widths and a high Eddington ratio appear to be necessary but not sufficient conditions for extreme Fe II emission, while the [O III]/Hβ_{NLR} ratio represents a more reliable diagnostic of such objects. Additionally, these objects exhibit a different slope in the FWHM Fe II – L_{5100} relation relative to the rest of the sample, implying a distinct physical origin and pointing towards an underlying AGN dichotomy.
5. The results indicate a possible stratification of the Fe II emission region occurring in sources with very strong Fe II emission. A high Eddington ratio may induce structural changes in the disc and BLR, resulting in a softening of the ionising continuum or the appearance of strong outflows that enhance collisional excitation. This can lead to the development of localised emission regions with specific physical conditions favourable to activating additional atomic processes. These processes could be responsible for the increase of the Fe II$_{incons}$ lines and Fe II$_{ILR}$ components and consequently for the enhancement of the observed Fe II strength.

Future research should be devoted to a more careful consideration of the possible atomic processes and physical conditions that could be responsible for the emission of additional Fe II components. Understanding the origin of the enhanced Fe II emission is essential for gaining better insight into the complex physics and structure of the BLR.

Acknowledgements. We thank the anonymous referee for valuable comments and suggestions that helped us to significantly improve the paper. This research was supported by the Ministry of Science, Technological Development and Innovation of the Republic of Serbia through contracts no. 451-03-33/2026-03/200002 and 451-03-33/2026-03/200162. Funding for the Sloan Digital Sky Survey IV has been provided by the Alfred P. Sloan Foundation, the U.S. Department of Energy Office of Science, and the Participating Institutions. SDSS-IV acknowledges support and resources from the Center for High Performance Computing at the University of Utah. The SDSS website is www.sdss4.org. SDSS-IV is managed by the Astrophysical Research Consortium for the Participating Institutions of the SDSS Collaboration including the Brazilian Participation Group, the Carnegie Institution for Science, Carnegie Mellon University, Center for Astrophysics|Harvard & Smithsonian, the Chilean Participation Group, the French Participation Group, Instituto de Astrofísica de Canarias, The Johns Hopkins University, Kavli Institute for the Physics and Mathematics of the Universe (IPMU)/University of Tokyo, the Korean Participation Group, Lawrence Berkeley National Laboratory, Leibniz Institut für Astrophysik Potsdam (AIP), Max-Planck-Institut für Astronomie (MPIA Heidelberg), Max-Planck-Institut für Astrophysik (MPA Garching), Max-Planck-Institut für Extraterrestrische Physik (MPE), National Astronomical Observatories of China, New Mexico State University, New York University, University of Notre Dame, Observatário Nacional/MCTI, The Ohio State University, Pennsylvania State University, Shanghai Astronomical Observatory, United Kingdom Participation Group, Universidad Nacional Autónoma de México, University of Arizona, University of Colorado Boulder, University of Oxford, University of Portsmouth, University of Utah, University of Virginia, University of Washington, University of Wisconsin, Vanderbilt University, and Yale University.

References

Ahumada, R., Allende Prieto, C., Almeida, A., Anders, F., et al. 2020, ApJS, 249, 3
Baldwin, J. A., Phillips, M. M., & Terlevich, R. 1981, PASP, 93, 5
Baldwin, J. A., Hamann, F., Korista, K. T., Ferland, G. J., Dietrich, M., & Warner, C. 2003, ApJ, 583, 649
Baldwin, J. A., Ferland, G. J., Korista, K. T., Hamann, F., & LaCluyze, A. 2004, ApJ, 615, 610
Bentz, M. C., Denney, K. D., Grier, C. J., Barth, A. J., et al. 2013, ApJ, 767, 149
Boroson, T. A. 2002, ApJ, 565, 78
Boroson, T. A., & Green, R. F. 1992, ApJS, 80, 109
Brotherton, M. S. 1994, ApJ, 430, 495B
Bruhweiler, F., & Verner, E. 2008, ApJ, 675, 83
Collin, S., & Joly, M. 2000, New Astron. Rev., 44, 531
Collin, S., Kawaguchi, T., Peterson, B. M., & Vestergaard, M. 2006, A&A, 456, 75
Collin-Souffrin, S., Dumont, S., Heidmann, N., & Joly, M. 1980, A&A, 83, 190
Denney, K. D. 2012, ApJ, 759, 44
Dong, X., Wang, T., Wang, J., et al. 2008, MNRAS, 383, 581
Dopita, M. A., Fischera, J., Sutherland, R. S., et al. 2006, ApJS, 167, 177
Du, P., & Wang, J.-M. 2019, ApJ, 886, 42
Fan, X., & Wu, Q. 2023, ApJ, 944, 159
Feltre, A., Charlot, S., & Gutkin, J. 2016, MNRAS, 456, 3354
Ferland, G. J., Done, C., Jin, C., Landt, H., & Ward, M. J. 2020, MNRAS, 494, 5917
Floris, A., Marziani, P., Panda, S., Śniegowska, M., et al. 2024, A&A, 689, A321
Ganci, V., Marziani, P., D'Onofrio, M., et al. 2019, A&A, 630, A110
Garnica, K., Negrete, C. A., Marziani, P., et al. 2022, A&A, 667, A105
Garnica, K., Dultzin, D., Marziani, P., & Panda, S. 2025, MNRAS, 540, 3289
Gaskell, C. M. 1985, ApJ, 291, 112
Gaskell, C. M., Thakur, N., Tian, B., & Saravanan, A. 2022, Astron. Nachr., 343, e210112
Goodrich, R. W. 1989, ApJ, 342, 224
Greene, J. E., & Ho, L. C. 2005, ApJ, 627, 721

Hamann, F., Korista, K. T., Ferland, G. J., Warner, C., & Baldwin, J. 2002, ApJ, 564, 592
Howarth, I. D. 1983, MNRAS, 203, 301
Hu, C., Wang, J.-M., Ho, L. C., et al. 2008, ApJ, 683, L115
Huang, J., Lin, D. N. C., & Shields, G. 2023, MNRAS, 525, 5702
Ilić, D., Rakić, N., & Popović, L. Č. 2023, ApJS, 267, 19
Joly, M. 1981, A&A, 102, 321
Joly, M. 1987, A&A, 184, 33
Kaspi, S., Smith, P. S., Netzer, H., Maoz, D., Jannuzi, B. T., & Giveon, U. 2000, ApJ, 533, 631
Kauffmann, G., Heckman, T. M., Tremonti, C., et al. 2003, MNRAS, 346, 1055
Kovačević, J., Popović, L. Č., & Dimitrijević, M. 2010, ApJS, 189, 15
Kovačević-Dojčinović, J., & Popović, L. Č. 2015, ApJS, 221, 35
Kovačević-Dojčinović, J., Dojčinović, I., Lakićević, M., & Popović, L. Č. 2022, A&A, 659, A130
Kovačević-Dojčinović, J., Dojčinović, I., Lakićević, M., & Popović, L. Č. 2025, A&A, 694, A289
Kubota, A., & Done, C. 2018, MNRAS, 480, 1247
Kwan, J., & Krolik, J. H. 1981, ApJ, 250, 478
Li, Z., Zhou, H., Hao, L., Wang, H., et al. 2015, ApJ, 812, 99
Lípari, S. L., & Terlevich, R. J. 2006, MNRAS, 368, 1001
Liu, Y.-S., & Bian, W.-H. 2022, ApJ, 937, 82
Marinello, M., Rodriguez-Ardila, R., Marziani, P., Sigut, A., & Pradhan, A. 2020, MNRAS, 494, 4187
Marziani, P., & Sulentic, J. W. 2014, MNRAS, 442, 1211
Marziani, P., Sulentic, J. W., Zwitter, T., Dultzin-Hacyan, D., & Calvani, M. 2001, ApJ, 558, 553
Marziani, P., Dultzin, D., Sulentic, J. W., et al. 2018, FrASS, 5, 6
Marziani, P., Garnica Luna, K., Floris, A., et al. 2025, Universe, 11, 69
Negrete, C. A., Dultzin, D., Marziani, P., & Sulentic, J. W. 2012, ApJ, 757, 62
Netzer, H. 1980, ApJ, 236, 406
Netzer, H., Shemmer, O., Maiolino, R., et al. 2004, ApJ, 614, 558
Osterbrock, D., & Ferland, G. 2006, Astrophysics of gaseous nebulae and active galactic nuclei (Sausalito, CA: University Science Book)
Osterbrock, D. E., & Pogge, R. W. 1985, ApJ, 297, 166
Panda, S. 2024, FrASS, 11, 1479874
Panda, S., Czerny, B., Adhikari, T. P., Hryniewicz, K., et al. 2018, ApJ, 866, 115
Panda, S., Czerny, B., Done, C., & Kubota, A. 2019b, ApJ, 875, 133
Panda, S., Marziani, P., & Czerny, B. 2019a, ApJ, 882, 79
Pandey, A., Martínez-Aldama, M. L., Czerny, B., et al. 2025, ApJS, 277, 36
Park, D., Barth, A. J., Ho, L. C., & Laor, A. 2022, ApJS, 258, 38
Peterson, B. M., Ferrarese, L., Gilbert, K. M., Kaspi, S., et al. 2004, ApJ, 613, 682
Popović, L. Č., & Kovačević, J. 2011, ApJ, 738, 68
Popović, L. Č., Kovačević-Dojčinović, J., Dojčinović, I., & Lakićević, M. 2023, A&A, 679, A34
Rakshit, S., & Woo, J.-H. 2018, ApJ, 865, 5
Schlegel, D. J., Finkbeiner, D. P., & Davis, M. 1998, ApJ, 500, 525
Sexton, R. O., Matzko, W., Darden, N., Canalizo, G., & Gorjian, V. 2021, MNRAS, 500, 2871
Shapovalova, A. I., Popović, L. Č., Burenkov, A. N., et al. 2012, ApJS, 202, 10
Shen, Y., & Ho, L. C. 2014, Nature, 513, 210
Sigut, T. A. A., & Pradal, A. K. 1998, ApJ, 499, L139
Śniegowska, M., Marziani, P., Czerny, B., et al. 2021, ApJ, 910, 115
Sulentic, J. W., Zwitter, T., Marziani, P., & Dultzin-Hacyan, D. 2000a, ApJ, 536, L5
Sulentic, J. W., Marziani, P., & Dultzin-Hacyan, D. 2000b, ARA&A, 38, 521
Sulentic, J. W., Marziani, P., Zamanov, R., et al. 2002, ApJ, 566, L71
Sulentic, J. W., Bachev, R., Marziani, P., Negrete, A. C., & Dultzin, D. 2007, ApJ, 666, 757
Sulentic, J. W., Marziani, P., & Zamfir, S. 2011, Balt. Astron., 20, 427
Sun, J., & Shen, Y. 2015, ApJ, 804, L15
Temple, M. J., Ferland, G. J., Rankine, A. L., Chatzikos, M., & Hewett, P. C. 2021, MNRAS, 505, 3247
Vanden Berk, D. E., Shen, J., Yip, C.-W., et al. 2006, AJ, 131, 84
Véron-Cetty, M.-P., Véron, P., & Gonçalves, A. C. 2001, A&A, 372, 730
Véron-Cetty, M.-P., Joly, M., & Véron, P. 2004, A&A, 417, 515
Wang, J. M., Ge, J. Q., Hu, C., et al. 2011, ApJ, 739, 3
Wang, J., Du, P., Hu, C., et al. 2014, ApJ, 793, 108
Wang, J. M., Zhai, S., Li, Y. R., et al. 2023, ApJ, 954, 84
Wills, B. J., Netzer, H., & Wills, D. 1985, ApJ, 288, 94
Wolf, J., Bañados, E., Fan, X., et al. 2026, A&A, 707, A299
Woo, J.-H., Bae, H.-J., Son, D., & Karouzos, M. 2016, ApJ, 817, 108
Wu, X.-B., & Liu, F.-K. 2004, ApJ, 614, 91
Yip, C. W., Connolly, A. J., Szalay, A. S., et al. 2004a, AJ, 128, 585
Yip, C. W., Connolly, A. J., Vanden Berk, D. E., et al. 2004b, AJ, 128, 2603
Yu, L.-M., Zhao, B.-X., Bian, W.-H., Wang, C., & Ge, X. 2020, MNRAS, 491, 5881
Zhang, X., Wang, T., Ferland, G., He, Z., & Wang, Y. 2024, ApJ, 971, 6
Zheng, W., & Keel, W. C. 1991, ApJ, 382, 121
Zheng, W., & O'Brien, P. T. 1990, ApJ, 353, 433

Appendix A: Two-component model of Fe II lines

The two-component model of the broad emission lines, which assumes that the BLR consists of two subregions (ILR and VBLR), has been considered in many studies (see Hu et al. 2008; Li et al. 2015, and references therein). The ILR is assumed to be further away from the black hole comparing the VBLR, with line widths FWHM ∼ 2000 km s^{-1} (Brotherton 1994; Li et al. 2015), while the comparison of the widths of ILR and VBLR components in Hβ gives approximately two to three times wider VBLR components (Hu et al. 2008; Kovačević et al. 2010; Kovačević-Dojčinović & Popović 2015).

It is found that the Fe II lines are kinematically connected to the Hβ ILR components (Hu et al. 2008; Kovačević et al. 2010), which implies their ILR origin, while Kovačević et al. (2010) indicate that it is also possible that part of the Fe II emission originates from VBLR. On the other hand, several empirical studies of optical Fe II lines (Véron-Cetty et al. 2004; Dong et al. 2008; Bruhweiler & Verner 2008; Park et al. 2022), noticed that Fe II lines have a broader and narrower components in some spectra (see Appendix B in Kovačević-Dojčinović et al. 2025). Popović et al. (2023) showed that the set of model spectra constructed as different rates of the ILR/VBLR contribution in Hβ and Fe II lines could reproduce the quasar main sequence. This motivated us to apply a two-component Fe II model for this research where consistent Fe II lines are fitted with ILR and VBLR components that are not tied to the same components of the Hβ.

However, applying the two-component Fe II model to an already complex Fe II template with several free parameters raises questions about the reliability and uniqueness of the fit decomposition, especially in spectra with very broad Fe II lines. Similar to Hβ, the ILR component of the Fe II line is expected to be narrower than the VBLR component and to have a FWHM of approximately ∼2000 km s^{-1}, implying that the two-component model is not justified for spectra with very broad Fe II lines. Namely, in these spectra there are no clearly visible peaks of the Fe II lines, because the lines are very broad and overlap, forming smooth bumps, which do not show any indication of the existence of two distinct emission regions.

We tested the validity of using the two-component Fe II model for fitting the sources with different Fe II line widths by comparing the χ^2 values obtained with the two-component Fe II fit to those derived from the single-component Fe II fit. Both models were applied to the full sample, and the resulting χ^2 differences were plotted as a function of the Fe II line width estimated with the single-component Fe II model (FWHM Fe II$_{1G}$) (see Fig. A.1). It can be seen that, for large number of objects with narrower Fe II lines (FWHM Fe II$_{1G}$ < 5000 km s^{-1}), the Fe II fit is significantly improved with the two-component Fe II model. On the other hand, for most of objects with very broad Fe II lines (FWHM Fe II$_{1G}$ > 5000 km s^{-1}), adopting a two-component Fe II model does not lead to a significant improvement in the fit quality compared to a single-component model. Additionally, in approximately 37% of objects with FWHM Fe II$_{1G}$ > 5000 km s^{-1}, the two-component Fe II model is reduced to a single-component one, as the χ^2 minimisation routine discarded one of the components to achieve the best fit. Since for these objects the decomposition is identical to the single-component one, they are not included in Fig. A.1.

Therefore, we found that application of the two-component Fe II model is justified for spectra with Fe II widths smaller than FWHM Fe II$_{1G}$ ∼ 5000 km s^{-1}. On the other hand, for spectra with very broad Fe II lines FWHM Fe II$_{1G}$ > 5000 km s^{-1}, fitting with the Fe II two-Gaussian model is unreliable because it does not have a unique decomposition and does not improve the quality of the fit compared to the single-Gaussian model.

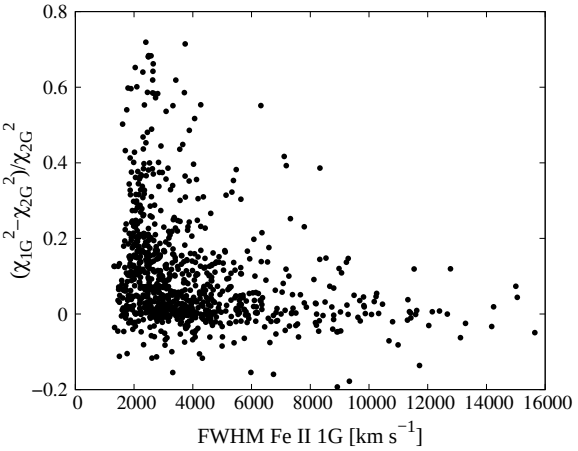

Fig. A.1. Comparison of the quality of fit of the Fe II$_{cons}$ lines with a single-Gaussian and two-Gaussian model (ILR+VBLR). On the Y-axis is the normalised difference between χ^2 of fit of Fe II$_{cons}$ with a single-Gaussian model (χ^2_{1G}) and two-Gaussian model (χ^2_{2G}). On the X-axis is the Fe II$_{cons}$ width, estimated using single-Gaussian model (FWHM Fe II$_{1G}$).

Appendix B: Distribution of the sources with different properties in the logλL_{5100} versus FWHM Fe II diagram

Since the gas outflows can play an important role in triggering different atomic processes, we examined the distribution of the outflow signatures within the logλL_{5100} versus FWHM Fe II diagram. Previous studies have shown that the wing component of the [O III] 5007 Å emission line is predominantly governed by non-gravitational outflow kinematics, while the [O III] core component traces both gravitational and outflow kinematics (Woo et al. 2016; Sexton et al. 2021; Kovačević-Dojčinović et al. 2022). In our fitting procedure, the [O III] lines are modelled with wing and core components. To trace the outflow kinematics, we used the shift of the [O III] wing components corrected for systemic shift of the narrow Balmer lines. We found that [O III] wing components with the largest blueshifts (<–400 km s^{-1}) are located in the left branch of the diagram (see Figure B.1).

We analysed the changes in the shape of the broad Hβ line across the logλL_{5100} versus FWHM Fe II plane by following the variations in the ratio of FWHM Hβ to the line dispersion of the total Hβ profile (FWHM Hβ/σ Hβ). Our results show that objects with lower values of this ratio are predominantly located in the left branch of the diagram (see Figure B.2). This may indicate differences in inclination or in BLR structure between objects from two branches.

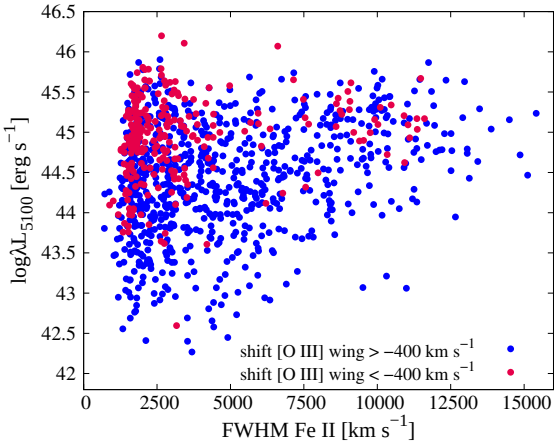

Fig. B.1. Outflow signatures in the logλL_{5100} versus FWHM Fe II plane. Red and blue points indicate sources with [O III] wing component shifts smaller and larger than -400 km s^{-1}, respectively.

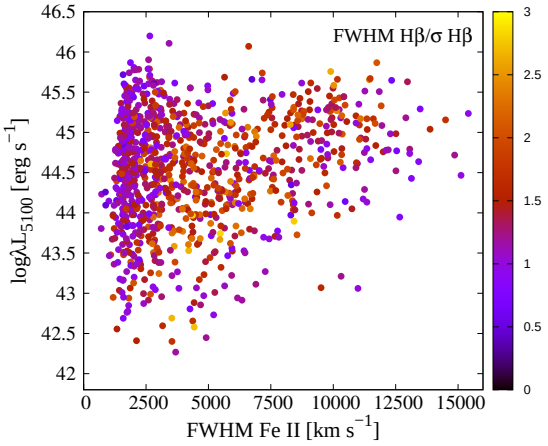

Fig. B.2. Variation of the FWHM Hβ/σHβ ratio across the logλL_{5100} versus FWHM Fe II parameter space. The colour scale indicates the value of the FWHM Hβ/σHβ ratio.